DOI: https://doi.org/10.2138/am-2022-8755. http://www.minsocam.org/

Revision 1

Word Count: 10348

Genesis of Mesozoic high-Mg dioritic rocks from the eastern North China Craton: Implications for the evolution of continental lithosphere

Jun Guo[1,2], Xiao-Long Huang[1,2]*, Peng-Li He[1], Lin-Li Chen[1], Jun-Wei Zhong[3]

[1]State Key Laboratory of Isotope Geochemistry, CAS Center for Excellence in Deep Earth Science, Guangzhou Institute of Geochemistry, Chinese Academy of Sciences, Guangzhou 510640, China

[2]Southern Marine Science and Engineering Guangdong Laboratory (Guangzhou), Guangzhou 511458, China

[3]Faculty of Land Resources Engineering, Kunming University of Science and Technology, Kunming 650000, Yunnan, China

*Corresponding author. Xiao-Long Huang, Tel.: (+86) 20-85290010

E-mail address: xlhuang@gig.ac.cn (Xiao-Long Huang)

ABSTRACT

Pre-Cenozoic High-Mg andesites (HMAs) are mostly present in continental interiors, but their genetic relationship with the continental lithosphere evolution remains unclear because of uncertainties of their mantle source, magmatic processes, and physicochemical conditions of formation. Early Cretaceous high-Mg dioritic rocks (HMDs, analogues of HMAs) of the Jinling complex in the Luxi area are typical intra-plate intrusions of the eastern North China Craton (NCC) and can be subdivided into two groups (Group-I and -II) on the basis of their petrographic and geochemical features. Group-I HMDs show low SiO_2 contents (52.47–56.10 wt%) and Sr/Y (34.5–39.6) and $(La/Yb)_N$ (10.3–13.6) ratios but high contents of MgO (7.86–9.13 wt%), Y (18.3–20.3 ppm), Yb (1.43–1.47 ppm), and compatible elements (Cr = 407–585 ppm; Ni = 117–216 ppm), classifying as sanukitic rocks. Group-II HMDs are characterized by high SiO_2 contents (63.81–64.87 wt%) and Sr/Y (47.1–63.4) and $(La/Yb)_N$ (16.1–17.5) ratios with low MgO (2.90–3.08 wt%), Y (0.88–1.04 ppm), Yb (0.88–1.04 ppm), and compatible elements (Cr = 201–213 ppm; Ni = 55–57 ppm) contents, belonging to adakitic rocks. Group-I and Group-II HMDs of the Jinling complex are closely related in spatial and temporal distribution, and all have enriched Sr-Nd isotopic compositions and arc-like trace elements patterns with abundant hydrous minerals. Therefore, the Jinling HMDs should share a common source of ancient sub-continental lithospheric mantle that had been metasomatized by aqueous fluids derived from the subducted Paleo-Pacific slab. The Jinling HMDs were not formed from interaction between slab-derived melts and mantle-wedge peridotites but were instead derived from partial melting of hydrous mantle peridotites in continental interior of the eastern NCC. The distinctly different petrography, geochemistry, and mineralogy of the two groups of rocks resulted mainly from differing magmatic processes at crustal depths. Thus, Pre-Cenozoic intra-plate HMAs/HMDs are genetically distinct from Cenozoic HMAs that were mostly present in arc settings and generally represent juvenile crust growth. In a way, Archean tonalitic-trondhjemitic-granodioritic rocks (TTG) and sanukitoids, geochemically similar to HMAs/HMDs, could also be derived from interaction between slab-derived melts and mantle-wedge peridotites in arc settings or partial melting of hydrous mantle peridotites in continental interiors, and thus might not always be related with continental crustal growth and the onset of plate subduction.

Key words: High-Mg dioritic rocks; Magmatic processes; Fluid metasomatism; Sub-Continental lithospheric mantle; North China Craton.

INTRODUCTION

The bulk composition of continental crust has been estimated to include 57–64 wt% SiO_2, 4.4–6.7 wt% Na_2O + K_2O, and 3.2–4.7 wt% MgO and to have Mg# [= 100 × $Mg^{2+}/(Mg^{2+} + Fe^{total})$] of 45–55 (e.g., Rudnick 1995; Rudnick and Gao 2014). Cenozoic HMAs have similar compositional characteristics to the bulk crust (e.g., Kelemen 1995). Despite their small magmatic volumes in modern subduction zones, Cenozoic HMAs have attracted considerable research attention during the past three decades because they can provide insights into the geodynamics of continental growth and the onset of plate tectonics, for their compositional similarities to Archean TTG and sanukitoids (e.g., Shirey and Hanson 1984; Kelemen 1995; Rudnick 1995; Tatsumi 2001, 2008; Martin et al. 2005; Wang et al. 2020a; Xu et al. 2020). Cenozoic HMAs can be categorized into four sub-types on the basis of their petrographic and geochemical characteristics, i.e., adakitic, bajaitic, sanukitic, and boninitic HMAs (e.g., Yogodzinski et al. 1995; Kemei et al. 2004; Tang and Wang 2010; Wang et al. 2020a). These sub-types are generated through different mechanisms and have distinct implications for slab–mantle interaction at modern convergent plate margins. Cenozoic HMAs occur mainly in oceanic subduction zones and subordinately in continental collision zones away from intracontinental settings (e.g., Defant and Drummond 1990; Yogodzinski et al. 1994, 1995; Tatsumi 2001, 2008; Wang et al. 2020a; Xu et al. 2020). However, Pre-Cenozoic HMAs, including Archean TTG and sanukitoids, have also been reported in continental interiors, such as the eastern NCC and the Central Asian orogenic belt (e.g., Gao et al. 2004; Yang et al., 2012a, 2012b; Wang et al. 2020a). Compared with the well-developed understanding of Cenozoic HMAs in arc settings, the nature and genesis of Pre-Cenozoic intra-plate HMAs remain unclear, including the mantle source, magmatic processes, and physicochemical conditions of formation.

Early Cretaceous HMDs are widely distributed in the eastern NCC (Fig. 1), which had

DOI: https://doi.org/10.2138/am-2022-8755. http://www.minsocam.org/

undergone a significant lithospheric thinning and destruction in Mesozoic with a thick and cold Paleozoic sub-continental lithospheric mantle (SCLM) replaced by a thin and hot Cenozoic SCLM (e.g., Menzies et al., 1993; Xu, 2001; Gao et al. 2004; Huang et al. 2012; Yang et al. 2021). These rocks generally have high contents of compatible elements and high Mg# values, and typically display arc-like trace-element characteristics, i.e., enrichment in light rare earth elements (REE) and large-ion lithophile elements (LILE) and depletion in high-field-strength elements (HFSE) and heavy REE, and enriched radiogenic isotope compositions (e.g., Yang et al. 2012a, 2012b; Jin et al. 2015; Lan et al. 2019; Sun et al. 2019; Gao et al. 2021; Zhang et al. 2021). Although their whole-rock major and trace element features are similar to those of Cenozoic HMAs, the Early Cretaceous HMDs are commonly considered to have been generated in an intracontinental setting during the Mesozoic descratonization of the eastern NCC (e.g., Gao et al. 2004; Yang et al. 2012a, 2012b; Jin et al. 2015; Lan et al. 2019; Sun et al. 2019; Gao et al. 2021; Zhang et al. 2021; Guo et al. 2022). However, the origin of the Mesozoic intra-plate HMDs remains controversial, with four main models having been proposed: interaction between delaminated lower continental crust-derived melts and mantle peridotites (e.g., Gao et al. 2004; Yang et al. 2006; Zhang et al. 2010; Jin et al. 2015); partial melting of enriched lithospheric mantle metasomatized by felsic melts derived from the delaminated lower continental crust or the subducted continental crust (e.g., Yang et al. 2012a, 2012b; Lan et al. 2019; Gao et al. 2021); magma mixing between crust-derived felsic melts and mantle-derived mafic melts (e.g., Chen et al. 2013) and assimilation of mantle peridotite by monzodioritic magmas at crustal depths (e.g., Qian and Hermann 2010). Here, we present whole-rock element and isotopic data and in situ mineral (amphibole and plagioclase) compositions for the Jinling intrusions in the Luxi region, typical intra-plate HMDs of the eastern NCC, where the SCLM might have been affected by the subducted Yangtze continental crust in Triassic or the subducted Paleo-Pacific oceanic crust in

Jurassi-Cretaceous. The objective of the study was to investigate the magma sources, magmatic processes, and associated physicochemical conditions of the Jinling HMDs to gain insights into the petrogenesis and geodynamics of intra-plate HMAs and their role in the evolution of continental lithosphere.

GEOLOGICAL SETTING AND SAMPLE DESCRIPTIONS

The NCC is bounded by the early Paleozoic Qilianshan Orogen to the west, the Paleozoic Central Asian orogenic belt to the north, and the Qinling–Dabie–Sulu orogenic belt to the south and the east, respectively (Fig. 1a; e.g., Zhao et al. 2005; Zheng et al. 2013). The NCC is subdivided into the Eastern and Western blocks by the Trans-North China Orogen (e.g., Zhao et al. 2005). The eastern NCC, lying to the east of the Daxinganling–Taihangshan Gravity Lineament (DTGL), underwent intensive tectono-magmatic activities during the Mesozoic and also pronounced lithospheric thinning (e.g., Menzies et al. 1993; Gao et al. 2004; Xu et al. 2004; Zhu et al. 2011; Huang et al. 2012; Yang et al. 2021). Shandong Province in the central part of the eastern NCC is separated by the Tan–Lu fault zone (TLFZ) into two parts (Fig. 1a and b), i.e., the Luxi block and the Jiaodong Peninsula (e.g., Huang et al. 2012).

The crystalline basement in the Luxi area is composed chiefly of Neoarchean Taishan Group TTG gneisses, which is unconformably overlain by Cambrian to Lower–Middle Ordovician clastic–carbonate successions. Late Carboniferous to Triassic marine–terrigenous-facies sedimentary rocks unconformably overlie Lower–Middle Ordovician limestones (Liu et al. 1996). Jurassic to Cretaceous terrestrial clastic rocks are unconformably overlain by Cenozoic strata composed predominantly of alluvial and lacustrine sediments (Song 2008). In addition to Precambrian magmatic rocks, voluminous Mesozoic intrusions are widespread in the Luxi area and represent two stages of magmatism; i.e., Early to Middle Jurassic monzonitic–syenitic magmatism (ca. 160–155 Ma) and more extensive Early Cretaceous gabbrodioritic–dioritic–monzonitic magmatism (ca. 132–112 Ma; e.g., Xu et al. 2004; Huang et al. 2012; Zhong and Huang 2012; Jin et al. 2015; Gao et al. 2021; Zhang et al. 2021).

The Jinling high-Mg dioritic complex is located in the Luxi area (Fig. 1b) and consists of a main body with several separate stocks that intruded Ordovician limestone and dolomite sequences of the Majiagou Formation (Fig. 1c; e.g., Zhong and Huang 2012). This complex is extensively covered by Quaternary deposits, meaning that it is difficult to observe the nature of contacts between different types of constituent rock. The Jinling HMDs have generally been subdivided into Group-I and Group-II HMDs in previous studies (e.g., Yang et al. 2006, 2012a, 2012b; Zhong and Huang 2012; Jin et al. 2015; Gao et al. 2021; Zhang et al. 2021; Guo et al. 2022). Group-I HMDs consist of gabbroic diorite and hornblende diorite, whereas Group-II HMDs are monzonite. This subdivision is followed in this study.

Seven gabbroic diorite, one hornblende diorite, and two monzonite samples were collected from the Jinling complex for whole-rock geochemical and mineral electron microprobe analyses. The gabbroic diorites are fresh and show porphyritic texture (Fig. 2a–c), with phenocrysts of orthopyroxene (5–10 vol%), clinopyroxene (5–10 vol%), amphibole (~5 vol%), and biotite (~5 vol%), and a matrix that is composed mainly of fine-grained plagioclase (30–35 vol%), amphibole (15–20 vol%), K-feldspar (~10 vol%), biotite (~5 vol%), and clinopyroxene (~5 vol%), with accessory minerals of magnetite, apatite, and zircon. Orthopyroxene and clinopyroxene phenocrysts are generally replaced by amphibole in rims (Fig. 2a–c), and amphibole phenocrysts show complex compositional zoning (Fig. 2d). The hornblende diorites also show porphyritic texture with amphibole phenocrysts of 20–25 vol% (Fig. 2d). The matrix consists primarily of fine-grained plagioclase (40–45 vol%), amphibole

This is the peer-reviewed, final accepted version for American Mineralogist, published by the Mineralogical Society of America.
The published version is subject to change. Cite as Authors (Year) Title. American Mineralogist, in press.
DOI: https://doi.org/10.2138/am-2022-8755. http://www.minsocam.org/

(15–20 vol%), K-feldspar (~5 vol%), and biotite (~5 vol%), with accessory minerals of magnetite, apatite, and zircon. The monzonites show porphyritic texture (Fig. 2e and f), with phenocrysts of plagioclase (~20 vol%) and amphibole (15–20 vol%), and a matrix that consists predominantly of fine-grained plagioclase (~15 vol%), amphibole (5–10 vol%), K-feldspar (30–35 vol%), and anhedral quartz (<5 vol%). Accessory minerals include magnetite, apatite, titanite, and zircon. Amphibole and plagioclase phenocrysts show complex compositional zoning (Fig. 2e and f). In the gabbroic and hornblende diorites, plagioclases appear only in the matrix and lack zoned texture (Fig. 2a–d). Magnetites are usually present around and/or are included in rims of amphibole phenocrysts and matrix amphiboles.

ANALYTICAL METHODS

Whole-rock major and trace elements

Whole-rock major elements were analyzed using a Rigaku RIX 2000 X-ray fluorescence spectrometer (XRF) at Guangzhou Institute of Geochemistry, Chinese Academy of Sciences (GIG-CAS), Guangzhou, China. The analytical uncertainties are mostly less than 2%. Whole-rock trace element concentrations were obtained by the Thermal X series 2 inductively coupled plasma-mass spectrometry (ICP-MS) equipped with a Cetac ASX-560 AutoSampler at the Tongwei Analytical Technology Company (TATC), Guizhou, China, and the ICP-MS procedure for trace element analysis followed the protocols of Eggins et al. (1997), with modifications described in Kamber et al. (2003) and Li et al. (2005). The analytical precisions are better than 5% for most trace elements, estimated from analytical results of the USGS Rock References W-2a and BHVO-2 in the same measurement session.

Whole-rock Sr-Nd isotopes

The separation and purification procedures for the whole-rock Sr–Nd isotopes were performed at TATC. Chemical separation was performed by conventional ion-exchange techniques. The detailed chemical procedures are similar to those described in Pin et al. (1997), Deniel and Pin (2001) and Míková et al. (2007). Total procedure blanks are typically in the ranges of ≤ 100 pg for Sr and ≤ 60 pg for Nd.

The purified solution Sr and Nd isotope ratios were measured by a Neptune Plus MC-ICP-MS at GIG-CAS. The analytical precisions of isotopic ratio were reported as 2σ standard errors. Normalizing factors of $^{86}Sr/^{88}Sr$ = 0.1194 and $^{146}Nd/^{144}Nd$ = 0.7219 are used to correct the mass fractionations of Sr and Nd during the measurements, respectively. During the analytical sessions, the measured values for standards NBS987 Sr were $^{87}Sr/^{86}Sr$ = 0.710248±8 (2σ, n=8) and those for JNdi-1 Nd were $^{143}Nd/^{144}Nd$ = 0.512115±4 (2σ, n=9). Two USGS reference materials W-2a and BHVO-2 were also processed for Sr–Nd isotopes to monitor the analytical accuracy and gave ratios of 0.706957±10 and 0.703480±14 for $^{87}Sr/^{86}Sr$, respectively, and of 0.512509±10 and 0.512989±18 for $^{143}Nd/^{144}Nd$, respectively, which are in agreement with the recommended values by Fourny et al. (2016) within errors. The analytical procedures are principally similar to the description in Wei et al. (2002) and Liang et al. (2003).

Back-scattered electron (BSE) images and Electron microprobe analyses

BSE images of the amphibole and plagioclase crystals were captured using a Carl Zeiss SUPRA55SAPPHIRE Field Emission-Scanning Electron Microscope (SEM) at GIG-CAS. In situ major elemental analyses were obtained using a Cameca SXFive FE Electron Probe Microanalyzer (EPMA) at GIG-CAS. This EPMA is equipped with an electron optical column with field emission source, controlled by Cameca PeakSight software. An operating condition of 15 kV accelerating voltage and 20 nA beam current was used during the course of this study. A variable peak counting time (10–60 s) was designed based on the intensity of characteristic X-ray line and desired precision for the element. Calibration standards used for feldspar analyses were albite (Na), almandine (Mg), sanidine (Si, K), hematite (Fe), plagioclase (Ca), and Celestite (Sr). Calibration standards for amphibole analyses were jadeite (Na, Al), diopside (Si, Mg, Ca), orthoclase (K), rutile (Ti), Cr_2O_3 (Cr), hematite (Fe), rhodonite (Mn), topaz (F) and tugtupite (Cl) from SPI company. The PAP (Pouchou and Pichoir) procedure was used for matrix correction (Pouchou and Pichoir 1991). The detailed procedures are the same as those described in He et al. (2021).

RESULTS

All the whole-rock and mineral geochemical data are listed in Supplementary Tables S1–3.

Whole-rock major and trace elements

Whole-rock major and trace elements compositions for the Jinling HMDs are presented in Supplementary Table S1. These compositions overlap with previously published data in diagrams of major and trace elements (Figs. 3–5). Group-I HMDs have low contents of SiO_2 (52.47–56.10 wt%), Al_2O_3 (11.67–13.00 wt%) and K_2O + Na_2O (4.20–5.39 wt%), and they plot in the field of gabbro diorite in a total alkali versus silica (TAS) diagram (Table S1; Fig. 3a). Group-I HMDs also have high contents of MgO (7.86–9.13 wt%), total (T)Fe_2O_3 (8.63–10.97 wt%) and CaO (6.61–8.48 wt%) with high Mg# values (61.3–66.8). Compared with Group-I HMDs, Group-II HMDs have considerably higher contents of SiO_2 (63.81–64.87 wt%), Al_2O_3 (15.16–15.53 wt%) and K_2O + Na_2O (8.21–8.67 wt%), and they plot in the field of quartz monzonite in a TAS diagram (Table S1; Fig. 3a). Group-II HMDs also have much lower contents of MgO (2.90–3.08 wt%), TFe_2O_3 (2.40–3.66 wt%), and CaO (3.44–4.40 wt%). Despite their much lower MgO contents, Group-II HMDs show considerably variable Mg# values (61.1–71.8) that are comparable to those of Group-I HMDs. Both Group-I and

Group-II HMDs as classified as high-K calc-alkaline series, but Group-II HMDs have much higher K_2O contents than Group-I (Fig. 3b). In Harker diagrams of major element oxides or compatible elements versus MgO, Group-I and Group-II HMDs show roughly similar geochemical trends with a pronounced compositional gap in MgO contents (Fig. 4). For both Group-I and Group-II HMDs, the contents of CaO, P_2O_5, TiO_2, TFe_2O_3, and other compatible elements decrease with decreasing MgO content, whereas those of SiO_2 and Al_2O_3 increase. However, for most major and trace elements, the geochemical variations of Group-II HMDs are wider than those of Group-I HMDs.

The two groups of HMDs show highly fractionated chondrite-normalized REE patterns with weak/negligible Eu anomalies (Fig. 5a) and are characterized by enrichment in LILE, negative Nb–Ta–Ti anomalies, and positive Pb anomalies in primitive mantle normalized multi-element diagrams (Fig. 5b). Although the two groups have similar LREE contents, Group-II HMDs have considerably lower contents of middle and heavy REE (Fig. 5). Furthermore, Group-I HMDs have substantially higher Yb (1.43–1.47 ppm) and Y (18.3–20.3 ppm) contents but much lower $(La/Yb)_N$ (10.3–13.6) and Sr/Y (34.5–39.6) ratios than Group-II HMDs [Yb = 0.88–1.04 ppm, Y = 10.5–12.3 ppm, $(La/Yb)_N$ = 16.1–17.5, and Sr/Y = 47.1–63.4; N denotes the normalization values relative to chondrite.]. In addition, Group-I HMDs exhibit slight negative Eu anomalies (Eu/Eu* = 0.93–0.95), and Group-II HMDs display slightly positive Eu anomalies (Eu/Eu* = 1.03–1.17; Fig. 5) owing to their much higher plagioclase contents (Fig. 2). Furthermore, Group-I HMDs have much higher contents of compatible elements (Cr = 407–585 ppm, Ni = 117–216 ppm) but lower contents of LILE (Rb = 28.8–48.1 ppm, Ba = 592–1030 ppm) compared with Group-II HMDs (Table S1; Figs. 4g–i and 5b).

Whole-rock Sr–Nd isotopes

Whole-rock Sr–Nd isotopic compositions for the two groups of HMDs are listed in

Supplementary Table S1 and are plotted in Fig. 6c together with literature data. The studied samples commonly show enriched Sr–Nd isotopic compositions with distinct variations between the two groups. Group-I HMDs display variably low $(^{87}Sr/^{86}Sr)_i$ ratios (0.7048–0.7052) and small negative $\varepsilon_{Nd}(t)$ values (−6.61 to −3.75), with two-stage Nd model ages of 1.47–1.23 Ga. In contrast, Group-II HMDs show slightly higher $(^{87}Sr/^{86}Sr)_i$ ratios (0.7054–0.7055) and more negative $\varepsilon_{Nd}(t)$ values (−9.29 to −8.60), corresponding to substantially older two-stage Nd model ages of 1.69–1.63 Ga (Table S1; Fig. 6c).

BSE images and mineral geochemistry of amphibole and plagioclase

The major element compositions of amphibole and plagioclase from the two groups of HMDs are presented in Supplementary Tables S2–3 and Figs. 7c and 8c–d. As shown in the BSE images (Fig. 7a and b), plagioclases from the two groups of HMDs show distinctive crystal morphology and internal texture. Plagioclase phenocrysts from Group-II HMDs show complex inner core (core I)–outer core (core II)–mantle–rim zoning with variable lightness in different domains (Fig. 7b). Euhedral plagioclases in the matrix and outer cores and rims of plagioclase phenocrysts have similar darkness, and they are much darker than the inner cores and mantles of plagioclase phenocrysts from Group-II HMDs. The outer cores of plagioclase phenocrysts from Group-II HMDs show relict textures of disequilibrium reaction (Fig. 7b). Different domains in the plagioclase phenocrysts have highly variable anorthite (An) contents. Inner cores have the highest An contents (34.6%–41.9%) and are andesine in composition. In contrast, the rims of plagioclase phenocrysts and matrix plagioclases have low An contents (8.8%–13.4% and 7.7%–13.5%, respectively) and are albite or oligoclase (Fig. 7c), suggesting normal zoning of plagioclase phenocrysts overall. However, the outer cores of plagioclase phenocrysts have much lower An contents (11.1%–19.4%; Fig. 7c) relative to mantles (An = 22.0%–31.6%; Fig. 7c), indicating reverse zoning within plagioclase phenocrysts. The outer cores of plagioclase phenocrysts from Group-II HMDs are best interpreted to be relicts of crustal contamination, as indicated by their relict texture and similar compositional characteristics to plagioclases from Archean TTGs (e.g., Jahn et al. 1988). Group-I HMDs lack plagioclase phenocrysts (Fig. 7a) and contain fine-grained euhedral plagioclase in the matrix (Fig. 7a). Matrix plagioclases in Group-I HMDs have An contents of 22.2%–30.0% and plot in the fields of oligoclase and andesine (Table S2; Fig. 7c), similar to the mantles of plagioclase phenocrysts from Group-II HMDs.

Both phenocryst and matrix amphiboles are found in the two groups of HMDs. The fine-grained amphiboles in the matrix are homogeneous, whereas amphibole phenocrysts from Group-I and Group-II HMDs show core–rim and core–mantle–rim compositional zoning patterns, respectively (Fig. 8a and b). The cores of amphibole phenocrysts from the Group-I and Group-II samples exhibit similar major element compositions, showing the lowest SiO_2 contents (42.18–46.09 wt% and 43.66–44.90 wt%, respectively) and the highest Al_2O_3 (7.96–10.69 wt% and 9.26–11.50 wt%, respectively) and TiO_2 contents (1.75–3.51 wt% and 0.51–3.05 wt%, respectively) of all phenocryst domains, and most of them are pargasite (Fig. 8c). The rims of amphibole phenocrysts from the Group-I and Group-II HMDs are also compositionally similar to each other. These rims have higher SiO_2 contents (48.50–54.34 wt% and 51.11–53.39 wt%, respectively) and much lower Al_2O_3 (1.91–6.37 wt% and 2.79–4.64 wt%, respectively) and TiO_2 (0.58–1.38 wt% and 0.65–1.09 wt%, respectively) contents than the cores and are classified as magnesiohornblende (Fig. 8d). The mantles of amphibole phenocrysts from Group-II HMDs have contents of SiO_2 (44.55–46.97 wt%), Al_2O_3 (8.18–9.36 wt%), and TiO_2 (1.09–2.67 wt%) that are intermediate between those of cores and rims, and most of their compositions fall in the field of edenite (Fig. 8c). Thus, amphibole phenocrysts from the two groups of HMDs show normal compositional zoning overall. Matrix amphiboles in Group-I and Group-II HMDs are similar to the rims of amphibole phenocrysts in terms of their internal textures and major element contents (Table S3; Fig. 8d), indicating their formation under similar physicochemical conditions. However, subtle differences exist between Group-I and Group-II HMDs with respect to the internal textures and major element compositions of amphibole phenocrysts. For example, Group-II amphibole phenocrysts have mantles, whereas Group-I HMD amphibole phenocrysts do not have (Fig. 8a), suggesting that Group-II HMDs may have undergone more complex magmatic processes in the crustal magma chamber. In addition, amphiboles of all phenocryst domains from Group-II HMDs have considerably higher Na_2O contents than those from Group-I HMDs at given SiO_2 contents (Table S3).

Discussion

Classification of the Jinling high-Mg dioritic rocks

High-Mg andesite, as a special type of andesite, is generally characterized by high SiO_2 (>52 wt%) and high Mg# values (>45) as well as low FeO^T/MgO ratios (<1.5) (e.g., Yogodzinski et al. 1994, 1995; Kelemen 1995; Tatsumi 2001, 2008; Tang and Wang 2010; Wang et al. 2020a). In general, Cenozoic HMAs occur mainly in arc settings regardless of the different sub-types (i.e., adakitic, bajaitic, sanukitic, and boninitic) (e.g., Yogodzinski et al. 1994, 1995; Kemei et al. 2004; Tang and Wang 2010; Wang et al. 2020a). Cenozoic adakitic HMAs show high Sr/Y and $(La/Yb)_N$ ratios and formed through minor interaction between slab-derived melts and mantle peridotite (e.g., Kay 1978; Defant and Drummond 1990; Yogodzinski et al. 1995; Kemei et al. 2004; Tang and Wang 2010). Cenozoic sanukitic HMAs show similar REE patterns to those of adakitic rocks but have much higher MgO contents (e.g., Yogodzinski et al. 1994, 1995; Tatsumi 2001, 2008; Kemei et al. 2004; Tang and Wang 2010; Wang et al. 2020a). Bajaitic HMAs have approximately similar trace-element characteristics to those of adakitic rocks, except for their extreme enrichment in Sr and depletion in Rb (e.g., Rogers et al. 1985; Kemei et al. 2004). Boninitic HMAs are enriched in bronzite phenocrysts, glass matrix, and augite microlites but lacks plagioclase crystals, and they are characterized by SiO_2 > 52 wt%, MgO > 8 wt%, TiO_2 < 0.5 wt%, U-shaped REE patterns, and marked depletion in HFSEs and REEs (e.g., Kemei et al. 2004; Tang and Wang 2010; Wang et al. 2020a). Although Pre-Cenozoic HMAs/HMDs occur widely in continental interiors worldwide, most of them have approximately similar major and trace elements compositions to those of Cenozoic adakitic and sanukitic HMAs (e.g., Shirey and Hanson 1984; Martin et al. 2005; Jin et al. 2015; Lan et al. 2019; Sun et al. 2019; Gao et al. 2021; Zhang et al. 2021) with few resembling Cenozoic bajaitic and boninitic HMAs (e.g., Polat et al. 2002). Cenozoic adakitic and sanukitic HMAs show remarkable differences in petrography and whole-rock geochemistry (e.g., Yogodzinski et al. 1994, 1995; Kemei et al. 2004; Tang and Wang 2010; Wang et al. 2020a). In general, adakitic HMAs contain more feldspathic minerals and less mafic minerals, have much higher SiO_2 and LILE contents, higher Sr/Y and $(La/Yb)_N$ ratios, and much lower MgO (and Mg# values), compatible-element (i.e., V, Cr, and Ni), Y, and Yb contents compared with sanukitic HMAs (e.g., Yogodzinski et al. 1994, 1995; Kemei et al. 2004; Tang and Wang 2010).

Group-I HMDs of the Jinling complex have low SiO_2, but high MgO, TFe_2O_3, and CaO contents with high Mg# values, which are similar to Cenozoic sanukitic HMAs (Fig. 9a and b; e.g., Yogodzinski et al. 1994; Tatsumi 2001, 2008; Tang and Wang 2010; Wang et al. 2020a). Group-II HMDs also have high Mg# values but much higher contents of SiO_2 and K_2O + Na_2O, and substantially lower contents of MgO, TFe_2O_3 and CaO, and they are roughly comparable to the major-element compositions of Cenozoic adakitic HMAs worldwide (Fig. 9a and b; e.g., Yogodzinski et al. 1995; Kemei et al. 2004; Tang and Wang 2010; Wang et al. 2020a). Furthermore, Group-I HMDs show substantially higher Yb (1.43–1.47 ppm) and Y (18.3–20.3 ppm) contents but lower $(La/Yb)_N$ (10.3–13.6) and Sr/Y (34.5–39.6) ratios than those of Group-II HMDs (Yb = 0.88–1.04 ppm, Y = 10.5–12.3 ppm, $(La/Yb)_N$ = 16.1–17.5, and Sr/Y = 47.1–63.4; Table S1; Fig. 9). In diagrams of Sr/Y versus Y (Fig. 9c and d), the majority of Group-II samples plot in the fields of adakite and adakitic HMAs, whereas Group-I samples plot in and/or near the fields of island-arc volcanic rocks and sanukitic HMAs. In addition, Group-I HMDs have much higher compatible-element contents (V = 172–254 ppm, Cr = 407–585 ppm, and Ni = 117–216 ppm) but lower LILE contents (Rb = 28.8–48.1 ppm and Ba = 592–1030 ppm, and Pb = 8.58–22.0 ppm) compared with Group-II HMDs (Table S1; Figs. 4g–i and 5). Therefore, the Group-I and Group-II HMDs of the Jinling complex are geochemically classified as sanukitic and adakitic HMDs, respectively.

Generation of the Jinling high-Mg dioritic rocks: Magmatic processes and physicochemical conditions

Magmatic processes. The two groups of HMDs in the Jinling complex display different geochemical compositions (Table S1; Figs. 4 and 6), which suggests that they underwent different magmatic processes and/or differing degrees of magmatic evolution in the crustal magma chamber. Group-I HMDs show variable LREE contents (e.g., La) with uniform La/Sm ratios (Fig. 10a), indicating that their compositional variations were controlled mainly by fractional crystallization. Slight crustal contamination is also inferred to have been involved in the generation of Group-I HMDs. The chemical compositions of amphibole in igneous rocks have been widely used to determine magma sources (i.e., mantle or crust; e.g., Jiang and An 1984; Zhang et al. 2015; Sun et al. 2019). Although the absolute contents of major elements in amphibole to a certain extent depends on physical conditions of host melt (Ridolfi et al. 2010), there are good linear correlations between Si, Ti and Al in wide ranges of pressures (0–10 kbar) and temperatures (650–1075 °C; e.g., Putirka 2016). In particular, the Si/(Si + Ti + Al) ratio of amphibole is a reliable indicator of the source of host magma, with values of ≥0.775 for crust-derived amphibole and ≤0.765 for mantle-derived amphibole (e.g., Jiang and An 1984; Li et al. 2021). As shown in Fig. 11, the cores of amphibole phenocrysts from Group-I HMDs plot predominantly in the mantle source field, whereas the rims of amphibole phenocrysts and matrix amphiboles fall mainly in the crustal source and/or crust–mantle mixed source fields, suggesting that crustal involvement was mostly occurred in the latest stage of magma evolution. The cores of amphibole phenocrysts from Group-I HMDs have Si/(Si + Ti + Al) ratios of 0.74–0.81, whereas rims and matrix amphiboles show much higher Si/(Si + Ti + Al) ratios (0.85–0.95; Table S3). However, the effects of crustal contamination was negligible in the genesis of Group-I HMDs, as inferred from the narrow ranges of whole-rock elemental and isotopic compositions (Figs. 6c and 10a–b) and the absence of inherited Neoarchean zircons (e.g., Yang et al. 2012b; Zhong and Huang 2012).

The MgO contents of the Group-I and Group-II samples are positively related to contents of CaO, TiO_2, TFe_2O_3, and compatible elements and negatively related to SiO_2 and Al_2O_3 contents (Fig. 4), indicating pronounced fractional crystallization of mafic minerals (i.e., olivine, orthopyroxene, and clinopyroxene) and Fe–Ti oxides. However, the Group-II samples show a weak positive trend in the diagram of La/Sm versus La (Fig. 10a), indicating that their compositional variations cannot be explained primarily by fractional crystallization and suggesting that crustal contamination also played an important role in generating Group-II HMDs. In diagrams of Si–Ti–Al, TiO_2 versus Al_2O_3, and (Na + K) versus Al^{IV} (Fig. 11), the cores of amphibole phenocrysts from Group-II HMDs plot mostly in the mantle source field, mantles fall in the crust–mantle mixing source field, and rims and matrix amphiboles plot predominantly in the crustal source field, suggesting substantial crustal contamination in different stage of magma evolution. In addition, the Si/(Si + Ti + Al) ratios of amphiboles gradually increase from cores (0.757–0.775) to mantles (0.784–0.811) to rims and matrix amphiboles (0.892–0.934; Table S3), consistent with an increasing influence of crustal contamination during magma evolution. This interpretation is supported by the relict textures and low An contents of outer cores of plagioclase phenocryst from Group-II HMDs (Table S2; Fig. 7b and c). Crustal contamination can also account for the main patterns of variation in whole-rock geochemical and isotopic compositions of samples of Group-II HMDs (Figs. 6b–c and 10). Most Group-II HMD samples fall in the field of Taishan Group TTG gneisses (e.g., Jahn et al. 1998; Peng et al. 2013; Chen et al. 2020) in diagrams of La/Sm versus La and $(Hf/Sm)_N$ versus $(Ta/La)_N$ (Fig. 10a and b), consistent with the involvement of ancient crustal materials. In addition, samples from Group-II HMDs have higher $(^{87}Sr/^{86}Sr)_i$, $(La/Yb)_N$, and Sr/Y and lower $\varepsilon_{Nd}(t)$ values compared with Group-I HMDs (Fig. 10c and d), which suggests more substantial involvement of crustal materials during the generation of Group-II HMDs. The Taishan Group TTG gneisses, as the main components of crystalline basement in the Luxi area, are identified as the most likely candidate for the involvement of crust during magma evolution (Figs. 6b–c and 10; e.g., Jahn et al. 1988; Peng et al. 2013; Chen et al. 2020), as supported by the presence of inherited Neoarchean zircons in monzonites from the Jinling complex (e.g., Jin et al. 2015; Gao et al. 2021; Zhang et al. 2021).

Physicochemical conditions. Physicochemical conditions, such as melt water content (H_2O_{melt}), temperature (T), pressure (P), and oxygen fugacity (fO_2), commonly play an important role in controlling the paths of magmatic evolution and the petrographic and geochemical variations of genetically associated magmas (Richards 2011). By applying the thermobarometric formulations of Ridolfi et al. (2010), the major element compositions of amphibole can be used to calculate the H_2O_{melt}, T, and P conditions of the melts that formed amphibole-bearing calc-alkaline igneous rocks. The geochemical characteristics of amphiboles from the Jinling HMDs can be used to estimate these conditions. Jinling HMD amphiboles have Al# (= Al^{VI}/Al_T) values of <0.21, indicative of a magmatic origin (Table S3; Ridolfi et al. 2010). The physicochemical parameters calculated from the compositions of different domains of amphibole phenocrysts from Group-I HMDs are consistent with those from Group-II HMDs (Fig. 12), indicating a close genetic relationship between the two groups of rocks and suggesting that they formed under similar physicochemical conditions but underwent different magmatic processes. Cores of amphibole phenocrysts from Group-I and Group-II HMDs yield the highest crystallization temperatures (850–944 and 895–941 °C, respectively) and pressures (135–277 and 192–327 MPa, respectively) (Table S3; Fig. 12a). The rims of amphibole phenocrysts (as well as matrix amphiboles) from the two groups of HMDs show considerably lower crystallization temperatures (723–802 and 720–756 °C, respectively) and pressures (30–90 and 37–58 MPa, respectively) than the cores (Table S3; Fig. 12a).

The calculated crystallization pressures can be used to estimate the depths of magma chamber during magma evolution of the Jinling HMDs. Given an average density of the upper crust of $\rho = 2.7$ g/cm^3, the estimated crystallization depths for the cores of amphibole phenocrysts from Group-I and Group-II HMDs are 5.1–10.5 and 7.2–12.3 km, respectively, whereas those for the rims of amphibole phenocrysts (including matrix amphiboles) are 1.1–3.4 and 1.4–2.2 km, respectively (Table S3). Estimated T–P conditions for the mantles of amphibole phenocrysts in Group-II HMDs are 857–895 °C and 143–195 MPa, respectively, corresponding to a depth of 5.4–7.4 km, intermediate between the estimated depths for cores and rims. These results suggest that the Jinling HMDs underwent multi-stage evolution in crustal magma chambers located at different depths.

The oxygen fugacity and water contents of magma are also key controls on the magma evolution paths and compositional variations of igneous rocks (e.g., Ridolfi et al. 2008, 2010). The oxygen fugacity of host magma can be estimated from amphibole compositions by applying the formula proposed by Ridolfi et al. (2010). The calculated fO_2 of melts in equilibrium with cores of amphibole phenocrysts are relatively high (Fig. 12b; ΔNNO + 0.5 to

ΔNNO + 1.7 for Group-I HMDs and ΔNNO + 0.7 to ΔNNO + 1.7 for Group-II HMDs), and amphibole phenocryst rims and matrix amphiboles yield even higher fO_2 of equilibrium melts (Fig. 12b; ΔNNO + 2.1 to ΔNNO + 3.0 for Group-I HMDs and ΔNNO + 2.3 to ΔNNO + 3.0 for Group-II HMDs). These results reveal that the Jinling HMDs were formed in a relatively oxidizing environment and that the oxygen fugacity changed during the operation of magmatic processes at different crustal depths. Thus, both fractional crystallization and crustal contamination processes played important roles in the formation of the two groups of HMDs. Furthermore, King et al. (2000) proposed that the $Fe^{3+}/(Fe^{3+} + Fe^{2+})$ ratios of amphibole are a reliable indicator of (i.e., strongly positively related to) the oxygen fugacity of the host magma. The different domains of amphibole phenocrysts from the two groups of HMDs show different evolutionary trends in a diagram of $Fe^{3+}/(Fe^{3+} + Fe^{2+})$ versus ΔNNO (Fig. 12d). The rims of amphibole phenocrysts and matrix amphiboles in the two groups of HMDs show substantially higher $Fe^{3+}/(Fe^{3+} + Fe^{2+})$ ratios and ΔNNO values relative to cores, with mantles having intermediate values between them (Fig. 12d).

Water contents of host magma can be calculated from amphibole compositions on the basis of the formula proposed by Ridolfi et al. (2010). The estimated water contents of melts in equilibrium with cores of amphibole phenocrysts from Group-I and Group-II HMDs are higher (Fig. 12c; 3.6–4.5 and 3.6–5.3 wt%, respectively) than those of melts in equilibrium with rims of amphibole phenocrysts and matrix amphiboles (Fig. 12c; 2.9–3.9 and 2.3–3.2 wt%, respectively). These results imply that the parental magmas of the Jinling HMDs contained abundant water and that their mantle sources had been metasomatized by aqueous fluids. It is expected that the water content of a melt should increase with increasing SiO_2 content during magmatic evolution because H_2O behaves similarly to incompatible elements (e.g., Ridolfi et al. 2010). However, during magma ascent, the solubility of water in silicate melts decreases with decreasing pressure (Holtz et al. 1995). Fluid exsolution is a common phenomenon during late-stage magmatic evolution, and the escape of fluids will reduce water contents of host magma. The evolved magmas in equilibrium with the rims of amphibole phenocrysts and matrix amphiboles in the two groups of HMDs have lower water contents compared with the near-primary magmas in equilibrium with cores (Fig. 12c), which suggests that magmatic fluids might have escaped from shallow chambers during late-stage magmatic evolution.

Magma sources of the Jinling high-Mg dioritic rocks

Cenozoic HMAs in arc settings can be generated through different mechanisms and have been widely used to characterize slab–mantle interactions at convergent plate margins (e.g., Kay 1978; Rogers et al. 1985; Martin 1986; Defant and Drummond 1990; Yogodzinski et al. 1994, 1995; Tatsumi 2001, 2008; Martin et al. 2005; Wang et al. 2020a). In general, Cenozoic HMAs in oceanic subduction zones show depleted or slightly enriched Sr-Nd-Pb-Hf isotopic compositions in all cases (e.g., Defant and Drummond 1990; Yogodzinski et al. 1994, 1995; Tatsumi 2001, 2008; Wang et al. 2020a; Xu et al. 2020). In contrast, the Jinling HMDs display strongly enriched radiogenic isotopic compositions, suggesting that their mantle sources were distinct from those of Cenozoic HMAs in arc settings and that these rocks were derived from partial melting of ancient sub-continental lithospheric mantle rather than asthenospheric mantle (e.g., Yang et al. 2006, 2012a, 2012b; Zhong and Huang 2012; Jin et al. 2015; Lan et al. 2019; Gao et al. 2021; Zhang et al. 2021).

Despite the progress made by previous studies of the petrology and geochemistry of Mesozoic mafic–intermediate igneous rocks from the eastern NCC, uncertainty remains regarding the nature of their mantle sources, especially the nature and origin of metasomatic agents in the sub-continental lithospheric mantle of the eastern NCC (e.g., Gao et al. 2004; Xu et al. 2004; Yang et al. 2006, 2012b; Huang et al. 2012; Zhong and Huang 2012; Jin et al. 2015; Lan et al. 2019; Sun et al. 2019; Gao et al. 2021; Zhang et al. 2021). These mafic–

intermediate igneous rocks have been interpreted as being derived from partial melting of ancient sub-continental lithospheric mantle of the eastern NCC with minor but variable contributions from asthenospheric mantle (e.g., Xu 2001; Xu et al. 2004; Zhong and Huang 2012), or partial melting of enriched lithospheric mantle that had been metasomatized by felsic melts originating from subducted or delaminated continental crust (e.g., Gao et al. 2004; Yang et al. 2006, 2012a, 2012b; Jin et al. 2015; Lan et al. 2019; Gao et al. 2021). A recent geochemical study has suggested that Mesozoic sub-continental lithospheric mantle of the eastern NCC that had been metasomatized by aqueous fluids derived from subducted Paleo-Pacific oceanic crust during the Early–Middle Jurassic effectively preserved its original radiogenic Sr-Nd-Hf isotopic compositions (e.g., Niu 2005; Wang et al. 2020b).

Group-I HMDs show enriched Sr-Nd isotopic compositions resembling those of ancient sub-continental lithospheric mantle of the eastern NCC (Fig. 6c; e.g., Zhang and Yang 2007; Yang et al. 2009), indicating that they might have been derived from partial melting of ancient sub-continental lithospheric mantle of the eastern NCC but did not require previous metasomatism by felsic melts derived from subducted or delaminated continental crust materials. In addition, Group-I HMDs fall in or near the field of subduction zone fluid-related metasomatism in a diagram of $(Hf/Sm)_N$ versus $(Ta/La)_N$ (Fig. 10b), which is consistent with the occurrence of abundant hydrous minerals (amphibole and biotite) and arc-like geochemical characteristics (i.e., enrichment in LILEs and LREEs and depletion in HFSEs and HREEs). In contrast, Group-II HMDs show slightly more enriched whole-rock Sr–Nd and zircon Lu-Hf isotopic compositions in comparison with Group-I HMDs (Fig. 6b and c), indicating the involvement of more ancient continental crustal components in the genesis of the Group-II HMDs. TTG gneisses of the Taishan Group are the favored candidate for the crustal materials involved during magma emplacement on account of their relatively high $(^{87}Sr/^{86}Sr)_i$ and low $\varepsilon_{Nd}(t)$ values (e.g., Jahn et al. 1988; Peng et al. 2013; Chen et al. 2020).

Nevertheless, a possible role of asthenospheric mantle- and/or oceanic crust-derived melts in the generation of the Jinling HMDs cannot be completely precluded, given their distinctly higher $\varepsilon_{Hf}(t)$ values relative to ancient sub-continental lithospheric mantle in the eastern NCC (Fig. 6b; e.g., Zhong and Huang 2012; Zhang et al. 2021).

Genetic mechanisms of formation of the Jinling high-Mg dioritic rocks

The genetic mechanisms and geodynamics of Pre-Cenozoic HMAs/HMDs in continental interiors are hotly debated, in contrast to the more established understanding of Cenozoic HMAs in arc settings. For instance, at least four genetic models have been proposed to explain the generation of Mesozoic HMAs/HMDs in the eastern NCC, i.e., partial melts of delaminated continental lower crust interacting with mantle peridotites (e.g., Gao et al. 2004; Yang et al. 2006, 2012a; Jin et al. 2015), partial melting of enriched lithospheric mantle metasomatized by subducted or delaminated continental crust (e.g., Yang et al. 2012b; Lan et al. 2019; Gao et al. 2021), magma mixing between crustal- and mantle-derived melts (e.g., Chen et al. 2013) and assimilation of previously emplaced mantle peridotite by crust-derived melts at crustal depths (e.g., Qian and Hermann 2010).

The two groups of Jinling HMDs display similar crystallization ages (Fig. 6a), indicating a close petrogenetic relationship between them in the same tectonic setting. Group-I HMDs were likely derived from partial melting of ancient sub-continental lithosphere mantle that had been metasomatized by aqueous fluids from subducted oceanic crust but without the involvement of metasomatism or the interaction of felsic melts derived from subducted or delaminated continental crust. The cores of amphibole phenocryst from Group-I and Group-II HMDs plot predominantly in the mantle source field (Fig. 11), which further contradicts the model of partial melting of continental lower crust interacting with or assimilating mantle peridotites at mantle and/or crustal depths (e.g., Gao et al. 2004; Yang et al. 2006, 2012a; Qian and Hermann 2010; Jin et al. 2015). Furthermore, Group-I HMDs show a narrow range of Sr–Nd isotopic compositions that are similar to those of sub-continental lithospheric mantle of the eastern NCC (Fig. 6c), suggesting that continental crust-derived melts were only negligibly involved in the petrogenesis of these rocks. However, the sub-continental lithospheric mantle of the eastern NCC consists predominantly of harzburgite and dunite (e.g., Menzies et al. 1993; Niu 2005), which are refractory and hard to melt under normal mantle P–T–H_2O conditions. It is noted that melts in equilibrium with the cores of amphibole phenocrysts from the Jinling HMDs have high H_2O contents (Fig. 12c), which suggests that the mantle source had been metasomatized by aqueous fluids that were probably derived from subducted Paleo-Pacific oceanic crust. In addition, experiments have shown that sanukitic HMAs may represent near-primary magmas in equilibrium with upper-mantle peridotites at T = 1050–1150 °C and P = 10–15 kbar and under H_2O-rich conditions (e.g., Tatsumi and Ishizaka 1982; Kelemen 1995; Tatsumi 2008), and partial melting of peridotites under H_2O-rich conditions at uppermost-mantle pressures can produce high-Mg andesitic rather than basaltic melts (e.g., Kelemen 1995; Hirose 1997; Tatsumi 2001, 2008). Group-I HMDs of the Jinling complex show comparable compositions of major elements with the experimental HMAs melts (Fig. 9a and b; e.g., Hirose 1997). Collectively, the Group-I HMDs of the Jinling complex were derived from partial melting of sub-continental lithospheric mantle of the eastern NCC that had been metasomatized by aqueous fluids derived from the subducted Paleo-Pacific oceanic crust at relatively high-T, low-P, and H_2O-rich conditions (Fig. 13).

In continental interiors, crustal materials might be involved in the formation of mafic–intermediate igneous rocks through source mixing or the process of assimilation and fractional crystallization. The temporal and spatial relationships between Group-I and Group-II HMDs suggest that they likely shared a common mantle source, which is further supported by their overall similar Sr-Nd-Pb-Hf isotopic compositions and similar physicochemical conditions of primary melts (Fig. 6b and c; e.g., Yang et al. 2006, 2012a, 2012b; Zhong and Huang 2012; Jin et al. 2015; Lan et al. 2019; Zhang et al. 2021). However, the differences in petrography, geochemistry, and radiogenic isotopes between the two groups of HMDs (Figs. 2–6) suggest that they likely underwent different magmatic processes during their evolution in crustal levels. The compositional variation of Group-I HMDs was controlled mainly by fractional crystallization, with only minor involvement of crustal materials that mostly occurred in the latest stage of magma evolution (Fig. 13), while Group-II HMDs underwent far more complex and intensive magmatic processes, with more intensive fractional crystallization of mafic minerals and more extensive involvement of crustal materials. Furthermore, TTG gneisses of the Taishan Group in the Luxi area have much higher Sr/Y, $(La/Yb)_N$, and $(^{87}Sr/^{86}Sr)_i$ ratios and larger negative $\varepsilon_{Nd}(t)$ values than those of sub-continental lithospheric mantle of the eastern NCC (e.g., Jahn et al. 1988; Peng et al. 2013; Chen et al. 2020) and are therefore the favored candidate for the contribution of crustal materials into Group-II HMDs during magma emplacement (Figs. 6c and 10c–d). Collectively, Group-II HMDs were also produced by partial melting of sub-continental lithospheric mantle of the eastern NCC that had been metasomatized by aqueous fluids from subducted Paleo-Pacific oceanic crust but underwent more extensive fractional crystallization of mafic minerals and greater involvement of crustal materials that were probably derived from TTG gneisses of the Taishan Group in the Luxi area (Fig. 13).

IMPLICATIONS FOR THE EVOLUTION OF CONTINENTAL LITHOSPHERE

Petrogenesis of intra-plate HMAs

The association of basalt–andesite–dacite–rhyolite is the most widely distributed Cenozoic arc igneous rock association and is generally considered to be derived from partial melting of fluid-metasomatized peridotites in the mantle wedge and subsequent intra-crustal differentiation processes; i.e., crustal contamination and fractional crystallization (e.g., Wang et al. 2020a; Xu et al. 2020; Zheng et al. 2020). In addition to slab-derived fluids, metasomatism or interaction between slab-derived melts and mantle-wedge peridotites is also an important control on the source nature of Cenozoic arc magmatism (e.g., Wang et al. 2020a; Xu et al. 2020; Zheng et al. 2020). In subduction zones, basaltic oceanic crust, underlying peridotitic mantle, and overlying sediments can be effectively transported to sub-arc depths beneath arc volcanoes and are all potential source materials of arc igneous rocks. Cenozoic adakites, as a special type of arc magmatic rock, are generally produced by partial melting of metabasalts at high pressure within the stability fields of garnet and rutile but outside the stability field of plagioclase and are thus genetically associated with the subduction of young and warm oceanic lithosphere (e.g., Defant and Drummond 1990; Yogodzinski et al. 1995; Kemei et al. 2004; Martin et al. 2005; Tang and Wang 2010; Wang et al. 2020a). When adakitic melts are produced at the surface of a subducted slab, they may infiltrate and react with mantle-wedge peridotites during magma ascent. At low melt/rock ratios, adakitic melts would be completely consumed in metasomatic reactions with mantle wedge, producing mantle sources for sanukitic and/or bajaitic HMAs, whereas at high melt/rock ratios, they would become adakitic HMAs (e.g., Kay 1978; Yogodzinski et al. 1995; Rapp et al. 1999; Martin et al. 2005; Wang et al. 2020a; Xu et al. 2020). Accordingly, the study of the origin of Cenozoic HMAs in modern arc volcanoes is an important petrological topic with respect to young and warm oceanic subduction systems and has implications for the understanding of chemical geodynamics at convergent plate margins (e.g., Defant and Drummond 1990; Martin et al. 2005; Xu et al. 2020; Zheng et al. 2020).

Besides Cenozoic HMAs, numerous Pre-Cenozoic HMAs/HMDs are also reported in continental interiors, and their petrogenesis is keenly debated. Contrary to Cenozoic HMAs, Pre-Cenozoic intra-plate HMAs/HMDs generally have strongly enriched radiogenic Sr-Nd-Pb-Hf isotopic compositions, indicating that they were produced mainly by partial melting of enriched lithospheric mantle rather than asthenospheric mantle (e.g., Gao et al. 2004; Xu et al. 2004; Yang et al. 2006, 2012a, 2012b; Zhong and Huang 2012; Jin et al. 2015; Lan et al. 2019; Sun et al. 2019; Zhang et al. 2021). In this study, the Group-I and Group-II HMDs of the Jinling complex correspond geochemically to sanukitic and adakitic HMAs, respectively. However, both the Group-I and Group-II HMDs were derived from partial melting of sub-continental lithospheric mantle of the eastern NCC metasomatized by aqueous fluids from the subducted Paleo-Pacific slab and underwent variable and extensive fractional crystallization and incorporation of crustal materials. Thus, the Jinling HMDs are not related to the subduction of young and warm oceanic crust nor to the growth of continental crust at convergent plate margins.

Although the Jinling HMDs are commonly considered to have been emplaced into the upper continental crust during the Mesozoic lithospheric destruction of the eastern NCC (e.g., Yang et al. 2012a, 2012b; Zhong and Huang 2012; Jin et al. 2015; Lan et al. 2019; Guo et al. 2022), their radiogenic isotopic compositions resemble those of sub-continental lithospheric mantle of the eastern NCC (Fig. 6c; e.g., Zhang and Yang 2007; Yang et al. 2009). Since the Early-Middle Jurassic, the Paleo-Pacific plate has been subducted westward under the eastern Asian continental margin (e.g., Maruyama et al. 1997; Zheng et al. 2013). The subducted Paleo-Pacific oceanic crust would have undergone metamorphic dehydration and/or partial melting below sub-arc depths, and the resultant aqueous fluids and hydrous melts would have further modified sub-continental lithospheric mantle of the eastern NCC, which would not only have formed metasomatized mantle sources with high oxygen fugacities and water contents but also significantly changed the rheological properties of the cratonic lithospheric mantle. Subsequently, the fluid-metasomatized lithospheric mantle of the eastern NCC would have been heated and melted to form mafic-intermediate magmas as the asthenosphere upwelled in late Mesozoic (Fig. 13).

Implications for the evolution of continental lithosphere

Cenozoic adakitic HMAs are formed by slab melting and are the products of the most common parental magmas in modern arc volcanoes. Subduction of young and warm oceanic lithosphere is fundamental to the slab-melting genesis of Cenozoic HMAs in modern subduction systems (e.g., Kay 1978; Rogers et al. 1985; Defant and Drummond 1990; Yogodzinski et al. 1994, 1995; Tatsumi 2001, 2008; Martin et al. 2005; Wang et al. 2020a). On average, subducting oceanic lithosphere was much younger and hotter during the Archean than for modern Earth, and slab melting should therefore have been a common phenomenon during the Archean (e.g., Martin 1986). Neoarchean sanukitoids of the southwestern Superior Province, Canada are a typical example of Pre-Cenozoic HMAs and are geochemically analogous to Cenozoic HMAs in the Japanese Setouchi belt, and it has been proposed that they are derived from partial melting of mantle peridotites that had been metasomatized by aqueous fluids or hydrous melts of subducting oceanic slab (Shirey and Hanson 1984). Furthermore, Neoarchean sanukitoids and low-silica adakitic rocks are widely considered to develop in oceanic subduction environments and might be diagnostic petrological records for the onset of plate subduction and Archean continental crustal growth. For example, numerous studies have argued that oceanic subduction was occurring during the Archean (e.g., Shirey and Hanson 1984; Polat et al. 2002; Martin et al. 2005; Hastie et al. 2015) on the basis of geochemical similarities between Archean sanukitoids and Cenozoic HMAs. The key question associated with the timing of onset of plate subduction is whether Archean sanukitoids developed exclusively in oceanic subduction systems.

In oceanic subduction zones, the subduction of oceanic plate not only forms the mantle-wedge structure but also generates arc volcanic rocks at convergent plate margins (e.g., Zheng et al. 2020). Partial melting of subducting oceanic slabs and subsequent interaction between slab-derived melts and mantle-wedge peridotites can generate adakitic rocks and mantle sources for sanukitic and/or bajaitic HMAs (e.g., Rogers et al. 1985; Defant and Drummond 1990; Yogodzinski et al. 1995; Kemei et al. 2004; Martin et al. 2005; Wang et al. 2020a; Xu et al. 2020). As mentioned above, Group-I HMDs of the Jinling complex belong to sanukitic rocks, and their primary magmas were derived from partial melting of sub-continental lithospheric mantle; while Group-II HMDs of the Jinling complex as adakitic rocks were formed through crustal contamination and fractional crystallization of the primary magmas of Group-I HMDs rather than by partial melting of the subducted oceanic slab. Thus, there is no requirement for a relationship between slab-derived melts and the formation of Pre-Cenozoic HMAs. If so, Neoarchean sanukitoids cannot be simply used to infer the operation of oceanic subduction. Furthermore, the Archean mantle was 200–300 °C hotter than modern mantle, and its derivative komatiitic magmas commonly contained several percent water (e.g., Martin 1986; Grove et al. 2004; Sobolev et al. 2016). Therefore, although we cannot completely rule out the possibility of slab dehydration in the Archean, Neoarchean TTG and sanukitoids could have been derived from partial melting of hydrous mantle peridotites at high temperatures in within-plate settings and might have experienced different magmatic processes in crustal chambers. Indeed, Pre-Cenozoic intra-plate HMAs and their intrusive equivalents appear to have been more common during the Archean than on modern Earth (e.g., Shirey and Hanson 1984; Martin 1986; Polat et al. 2002; Martin et al. 2005).

However, Archean TTG, the primary rock type in Archean continental crust (Condie 2005), is compositionally similar to Cenozoic adakites (e.g., Defant and Drummond 1990; Martin et al. 2005). Some studies have compared the two rock types to establish the mechanisms of Archean continental crustal growth (Condie 2005; Martin et al. 2005). Archean TTGs were produced primarily through partial melting of a basaltic source under eclogite-facies conditions, which could have occurred either in subduction zones or at the base of thickened continental crust (e.g., Defant and Drummond 1990; Kay and Kay 1991; Martin et al. 2005; Wang et al. 2020a). In fact, the composition of Archean TTGs varied over time. In general, >3.5 Ga TTGs have lower Mg, Cr, Ni, and Sr content than <3.0 Ga TTGs that have high Mg, Cr, Ni, and Sr contents (Martin et al. 2005), which is considered to be related to a change in oceanic lithosphere subduction; i.e., >3.5 Ga TTGs lack a mantle-wedge compositional contribution, whereas <3.0 Ga TTGs record such a contribution (Martin et al. 2005). The Group-II HMDs of the Jinling complex have high contents of compatible elements (e.g., Ni = 55–57 ppm; Cr = 201–213 ppm) and MgO (2.90–3.08 wt%) with high Mg# (61.1–71.8) and slightly positive Sr anomalies (Table S1; Figs. 4a and 5b), which show similar geochemical characteristics to the <3.0 Ga TTGs (MgO = ~5 wt%; Mg# = ~65; Cr = ~200 ppm; Ni = ~70 ppm; slightly positive Sr anomalies; e.g., Martin and Moyen 2002; Martin et al. 2005). The petrogenesis of the Group-II HMDs implies that subduction and melting of oceanic slabs were not required to generate Pre-Cenozoic adakitic rocks. Accordingly, the geodynamics of widespread Archean TTGs in ancient cratons should be reconsidered when investigating the mechanisms of Archean continental crustal growth and for comparisons with Cenozoic adakites in modern arc settings.

CONCLUSIONS

The Early Cretaceous Jinling complex in the Luxi area of the eastern NCC can be subdivided into two groups of HMDs. Group-I HMDs, comprising gabbroic diorites and hornblende diorites, have geochemical features similar to those of Cenozoic sanukitic HMAs, whereas Group-II HMDs are monzonites and are geochemically classified as adakitic HMAs.

Group-I and Group-II HMDs of the Jinling complex share a common source of ancient sub-continental lithospheric mantle of the eastern NCC that had been metasomatized by fluids from subducted Paleo-Pacific slab. However, the two groups of HMDs show highly distinct petrographic and whole-rock geochemical characteristics as a result of different magmatic processes that occurred in the crustal magma chambers.

The two groups of HMDs of the Jinling complex were not formed by interaction between slab-derived melts and mantle-wedge peridotites but were instead derived from partial melting of hydrous mantle peridotites in continental interior of the eastern NCC.

Pre-Cenozoic intra-plate HMAs/HMDs may have had a different role in the evolution of continental lithosphere compared with Cenozoic HMAs in arc settings. Neoarchean sanukitoids and TTGs were produced by either interaction between slab-derived melts and mantle-wedge peridotites or partial melting of hydrous mantle peridotites.

ACKNOWLEDGMENTS

We appreciate L. Zhang for the assistance with whole-rock Sr-Nd isotope analysis. We are grateful to Prof. Chao Zhang and an anonymous reviewer, for their careful reviews and constructive comments, which considerably improved the manuscript. This work was financially supported by the National Natural Science Foundation of China (NSFC projects 42021002, 41625007) and the Key Special Project for Introduced Talents Team of Southern Marine Science and Engineering Guangdong Laboratory (Guangzhou) (GML2019ZD0202). This is contribution No. IS-XXXX from GIGCAS.

REFERENCES CITED

Chen, B., Chen, C.J., He, J.B., and Liu, A.K. (2013) Origin of Mesozoic high-Mg adakitic rocks from northeastern China: Petrological and Nd–Sr–Os isotopic constraints. Chinese Science Bulletin, 58, 1941–1953.

Chen, Y., Zhang, J., Liu, J., Han, Y.G., Yin, C.Q., Qian, J.H., and Liu, X.G. (2020) Crustal growth and reworking of the eastern North China Craton: Constraints from the age and geochemistry of the Neoarchean Taishan TTG gneisses. Precambrian Research, 343, 105706.

Condie, K.C. (2005) High field strength element ratios in Archean basalts: A window to evolving sources of mantle plumes? Lithos, 79, 491–504.

Defant, M.J., and Drummond, M.S. (1990) Derivation of some modern arc magmas by melting of young subducted lithosphere. Nature, 347, 662–665.

Deniel, C., and Pin, C. (2001) Single-stage method for the simultaneous isolation of lead and strontium from silicate samples for isotopic measurements. Analytica Chimica Acta, 426, 95–103.

Eggins, S. M., Woodhead, J. D., Kinsley, L. P. J., Mortimer, G. E., Sylvester, P., McCulloch, M. T., Hergt, J. M., and Handler, M. R. (1997) A simple method for the precise determination of ≥40 trace elements in geological samples by ICPMS using enriched isotope internal standardization. Chemical Geology, 134, 311–326.

Fourny, A., Weis, D., and Scoates, J.S. (2016) Comprehensive P b-Sr-Nd-Hf isotopic, trace element, and mineralogical characterization of mafic to ultramafic rock reference materials. Geochemistry, Geophysics, Geosystems, 17, 739–773.

Gao, S., Rudnick, R.L., Yuan, H.-L., Liu, X.-M., Liu, Y.-S., Xu, W.-L., Ling, W.-L., Ayers, J., Wang, X.-C., and Wang, Q.-H. (2004) Recycling lower continental crust in the North China craton. Nature, 432, 892–897.

Gao, J.L., Zhou, Y.G., Zhang, Z.F., Gao, M.B., Zhao, T.Q., Tian, Z.H., and Zhu, Z.H. (2021) Magma source and tectonic setting of Jinling pluton in eastern North China Craton: Evidences from petrography, petrogeochemistry and chronology. Chinese Journal of Geology, 56, 253–271 (in Chinese with English abstract).

Grove, T. L., and Parman, S. W. (2004) Thermal evolution of the Earth as recorded by komatiites. Earth and Planetary Science Letters, 219, 173–187.

Guo, J., Huang, X.L., He, P.L., Chen, L.L., and Zhong, J.W. (2022) Compositional variation of amphiboles from Mesozoic high-Mg diorites in western Shandong: Implications for mineralization of the skarn-type iron deposits. Submitted to Geotectonica et Metallogenia (in Chinese with English abstract).

Hastie, A.R., Fitton, J.G., Mitchell, S.F., Neill, I., Nowell, G.M., and Millar, I.L. (2015) Can fractional crystallization, mixing and assimilation processes be responsible for Jamaican-type Adakites? Implications for generating Eoarchaean continental crust. Journal of Petrology, 56, 1251–1284.

He, P.L., Huang, X.L., Yang, F., and Wang, X. (2021) Mineralogy Constraints on Magmatic Processes Controlling Adakitic Features of Early Permian High-magnesium Diorites in the Western Tianshan Orogenic Belt. Journal of Petrology, 61, 1–33.

Hirose, K. (1997) Melting experiments on lherzolite KLB-1 under hydrous conditions and generation of high-magnesian andesitic melts. Geology, 25, 42–44.

Holtz, F., Behrens, H., Dingwell, D. B., and Johannes, W. (1995) H_2O solubility in haplogranitic melts: compositional, pressure, and temperature dependence. American Mineralogist, 80, 94–108.

Huang, X.L., Zhong, J.W., and Xu, Y.G. (2012) Two tales of the continental lithospheric mantle prior to the destruction of the North China Craton: Insights from Early Cretaceous mafic intrusions in western Shandong, East China. Geochimica et Cosmochimica Acta, 96, 193–214.

Jahn, B.M., Auvray, B., Shen, Q.H., Liu, D.Y., and Zhang, Z.Q. (1988) Archean crustal evolution in China: the Taishan complex, and evidence for juvenile crustal addition from long-term depleted mantle. Precambrian Research, 38, 381–403.

Jiang, C.Y., and An, S.Y. (1984) On chemical characteristics of cal-cic amphiboles from igneous rocks and their petrogenesis significance. Journal of Mineralogy and Petrology, 3, 1–9 (in Chinese with English abstract).

Jin, Z.L., Zhang, Z.C., Hou, T., Santosh, M., and Han, L. (2015) Genetic relationship of high-Mg dioritic pluton to iron mineralization: A case study from the Jinling skarn-type iron deposit in the North China Craton. Journal of Asian Earth Sciences, 113, 957–979.

Kamber, B.S., Greig, A., Schoenberg, R., and Collerson, K.D. (2003) A refined solution to Earth's hidden niobium: implications for evolution of continental crust and mode of core formation. Precambrian Research, 126, 289–308.

Kamei, A., Owada, M., Nagao, T., and Shiraki, K. (2004) High-Mg diorites derived from sanukitic HMA magmas, Kyushu Island, southwest Japan arc: evidence from clinopyroxene and whole rock compositions. Lithos, 75, 359–371.

Kay, R.W. (1978) Aleutian magnesian andesites: Melts from subducted Pacific Ocean crust. Journal of Volcanology and Geothermal Research, 4, 117–132.

Kay, R. W., and Kay, S.M. (1991) Creation and destruction of lower continental crust. Geologische Rundschau, 80, 259–278.

Kelemen, P.B. (1995) Genesis of high Mg# andesites and the continental crust. Contributions to Mineralogy and Petrology, 120, 1–19.

King, P.L., Hervig, R.L., Holloway, J.R., Delaney, J.S., and Dyar, M.D. (2000) Partitioning of Fe3+/Fetotal between amphibole and basanitic melt as a function of oxygen fugacity. Earth and Planetary Science Letters, 178, 97–112.

LaFlèche, M.R., Camire, G., and Jenner, G.A. (1998) Geochemistry of post-Acadian, Carboniferous continental intraplate basalts from the Maritimes Basin, Magdalen islands, Quebec, Canada. Chemical Geology, 148, 115–136.

Lan, T.-G., Hu, R.-Z., Chen, Y.-H., Wang, H., Tang, Y.-W., and Liu, L. (2019) Generation of high-Mg diorites and associated iron mineralization within an intracontinental setting: Insights from ore-barren and ore-bearing intrusions in the eastern North China Craton. Gondwana Research, 72, 97–119.

Li, B. P., Greig, A., Zhao, J. X., Collerson, K. D., Quan, K. S., Meng, Y. H., and Ma, Z. L. (2005) ICP-MS trace element analysis of Song dynasty porcelains from Ding, Jiexiu and Guantai kilns, north China. Journal of Archaeological Science, 32, 251–259.

Li, J. L., Chen, Z. L., Zhou, T. F., Han, F. B., Zhang, W. G., Huo, H. L., Liu, B., Zhao, T. Y., Han, Q., Li, P., and Chen, G.M. (2021) Mineralogical characteristics of amphibole in Calc-alkalic intrusive rocks from the Juelotage tectonic belt of the Eastern Tianshan and its implication for regional prospecting. Geotectonica et Metallogenia, 45, 534–552 (in Chinese with English abstract).

Liang, X. R., Wei, G.J., Li, X.H., and Liu, Y. (2003) Precise measurement of $^{143}Nd/^{144}Nd$ and Sm/Nd ratios using multiple-collectors inductively couple plasma-mass spectrometer (MC-ICP-MS). Geochimica, 32, 91–96 (in Chinese with English abstract).

Liu, B.P., Quan, Q.Q., Feng, Q.L., Zhao, X.W., and Zhou, Z.G. (1996). Historical Geology of China. Geological Publishing House, pp. 1–277.

Maruyama, S., Isozaki, Y., Kimura, G., and Terabayashi, M. (1997) Paleogeographic maps of the Japanese Islands: Plate tectonic synthesis from 750 Ma to the present. Island Arc, 6, 121–142.

Martin, H. (1986) Effect of steeper Archean geothermal gradient on geochemistry of subduction-zone magmas. Geology, 14, 753–756.

Martin, H., and Moyen, J.-F. (2002) Secular changes in TTG composition as markers of the progressive cooling of the Earth. Geology, 30, 319–322.

Martin, H., Smithies, R.H., Rapp, R., Moyen, J.F., and Champion, D. (2005) An overview of adakite, tonalite-trondhjemite-granodiorite (TTG), and sanukitoid: relationships and some implications for crustal evolution. Lithos, 79, 1–24.

McDonough, W.F., and Sun, S.-S. (1995) Composition of the Earth. Chemical Geology, 120, 223–253.

Menzies M. A., Fan W. M., and Zhang M. (1993) Palaeozoic and Cenozoic lithoprobes and the loss of >120 km of Archaean lithosphere, Sino-Korean craton, China. In Magmatic Processes and Plate Tectonics (eds. H. M. Prichard, T. Alabaster, N. B. W. Harris and C. R. Neary). Geological Society Special Publication, 76, 71–78.

Míková, J., and Denková, P. (2007) Modified chromatographic separation scheme for Sr and Nd isotope analysis in geological silicate samples. Journal of Geosciences, 52, 221–226.

Niu, Y.L. (2005) Generation and Evolution of Basaltic Magmas: Some Basic Concepts and a New View onthe Origin of Mesozoic-Cenozoic Basaltic Volcanism in Eastern China. Geological Journal of China Universities, 11, 9–46.

Peng, T.P., Wilde, S.A., Fan, W.M., and Peng, B.X. (2013) Late Neoarchean potassic high Ba-Sr granites in the Taishan granite-greenstone terrane: Petrogenesis and implications for continental crustal evolution. Chemical Geology, 344, 23–41.

Pin, C., and Zalduegui, J.F.S. (1997) Sequential separation of light rare-earth elements, thorium and uranium by miniaturized extraction chromatography: application to isotopic analyses of silicate rocks. Analytica Chimica Acta, 339, 79–89.

Polat, A., Hofmann, A.W., and Rosing, M.T. (2002) Boninite-like volcanic rocks in the 3.7-3.8 Ga Isua greenstone belt, West Greenland: Geochemical evidence for intra-oceanic subduction zone processes in the early Earth. Chemical Geology, 184, 231–254.

Pouchou, J. L., and Pichoir, F. (1991) Quantitative-analysis of homogeneous or stratified microvolumes applying the model pap. Electron Probe Quantitation, 31–75.

Putirka, K. (2016) Amphibole thermometers and barometers for igneous systems and some implications for eruption mechanisms of felsic magmas at arc volcanoes. American Mineralogist, 101, 841–858.

Qian, Q., and Hermann, J. (2010) Formation of high-Mg diorites through assimilation of peridotite by monzodiorite magma at crustal depths. Journal of Petrology, 51, 1381–1416.

Rapp, R.P., Shimizu, N., Norman, M.D., and Applegate, G.S. (1999) Reaction between slab-derived melts and peridotite in the mantle wedge: experimental constraints at 3.8 GPa. Chemical Geology, 160, 335–356.

Richards, J.P. (2011) Magmatic to hydrothermal metal fluxes in convergent and collided margins. Ore Geology Reviews, 40, 1–26.

Ridolfi, F., Puerini, M., Renzulli, A., Menna, M., and Toulkeridis, T. (2008) The magmatic feeding system of El Reventador volcano (Sub-Andean zone, Ecuador) constrained by texture, mineralogy and thermobarometry of the 2002 erupted products. Journal of Volcanology and Geothermal Research, 176, 94–106.

Ridolfi, F., Renzulli, A., and Puerini, M. (2010) Stability and chemical equilibrium of amphibole in calc-alkaline magmas: an overview, new thermobarometric formulations and application to subduction-related volcanoes. Contributions to Mineralogy and Petrology, 160, 45–66.

Rogers. G., Saunders, A.D, Terrell, D.J., Verma, S.P., and Marriner, G.F. (1985) Geochemistry of Holocene volcanic rocks associated with ridge subduction in Baja California, Mexico. Nature, 315, 389–392.

Rudnick, R.L. (1995) Making continental crust. Nature, 378, 571–578.

Rudnick, R.L., and Gao, S. (2014) Composition of the Continental Crust, Treatise on Geochemistry, 4, pp. 1–51.

Shirey, S.B., and Hanson, G.N. (1984) Mantle-derived Archaean monozodiorites and trachyandesites. Nature, 310, 222–224.

Sobolev, A.V., Asafov, E.V., Gurenko, A.A., Arndt, N.T., Batanova, V.G., Portnyagin, M.V., Garbe-Schonberg, D., and Krasheninnikov, S.P. (2016) Komatiites reveal a hydrous Archaean deep-mantle reservoir. Nature, 531, 628–632.

Song, M.C. (2008) Tectonic Framework and Tectonic Evolution of the Shandong Province. Dissertation submitted to Chinese Academy of Geological Sciences, pp. 1–248 (in Chinese).

Sun, Y., Wu, T., Xiao, L., Bai, M., and Zhang, Y.H. (2019) Contrasting mineralogical-geochemical compositions of ore-bearing and ore-barren intrusive complexes in the Handan-Xingtai district, North China Craton: Implications for the iron mineralization. Lithos, 350–351, 105244.

Tang, G.J., and Wang, Q. (2010) High-Mg andesites and their geodynamic implications. Acta Petrologica Sinica, 26, 2495–2512 (in Chinese with English abstract).

Tatsumi, Y. (2001) Geochemical modeling of partial melting of subducting sediments and subsequent melt-mantle interaction: Generation of high-Mg andesites in the Setouchi volcanic belt, southwest Japan. Geology, 29, 323–326.

Tatsumi, Y. (2008) Making continental crust: The sanukitoid connection. Science Bulletin, 53, 1620–1633.

Tatsumi, Y., and Ishizaka, K. (1982) Origin of high-magnesian andesites in the Setouchi volcanic belt, southwest Japan, I. Petrographical and chemical characteristics. Earth and Planetary Science Letters, 60, 293–304.

Wang, Q., Hao, L.L., Zhang, X.Z., Zhou, J.S., Wang, J., Li, Q.W., Ma, L., Zhang, L., Qi, Y., Tang, G.J., Dan, W., and Fan, J.J. (2020a) Adakitic rocks at convergent plate boundaries: Compositions and petrogenesis. Science China Earth Sciences, 63, 1992–2016.

Wang, X.X., Xiao, Y.L., Sun, H., Wang, Y.Y., Liu, J.G., Yang, K., Gu, H.O., Hou, Z.H., Tian, Y., Wu, W.P., and Ma, Y.G. (2020b) Initiation of the North China Craton destruction: Constraints from the diamond-bearing alkaline basalts from Lan'gan, China. Gondwana Research, 80, 228–243.

Wei, G.J., Liang, X.R., Li, X.H., and Liu, Y. (2002) Precise measurement of Sr isotopic compositions of liquid and solid base using (LA) MCICP-MS. Geochimica, 31, 295–305 (in Chinese with English abstract).

Xu, Y.-G. (2001) Thermo-tectonic destruction of the Archaean lithospheric keel beneath the Sino-Korean Craton in China: Evidence, timing and mechanism. Physics and Chemistry of the Earth, Part A: Solid Earth and Geodesy, 26, 747–757.

Xu, Y.G., Huang, X.L., Ma, J.L., Wang, Y.-B., Iizuka, Y., Xu, J.F., Wang, Q., and Wu, X.Y. (2004) Crust-mantle interaction during the tectono-thermal reactivation of the North China Craton: constraints from SHRIMP zircon U-Pb chronology and geochemistry of Mesozoic plutons from western Shandong. Contributions to Mineralogy and Petrology, 147, 750–767.

Xu, Y.G., Wang, Q., Tang, G.J., Wang, J., Li, H.Y., Zhou, J.S., Li, Q.W., Qi, Y., Liu, P.P., Ma, L., and Fan, J.J. (2020) The origin of arc basalts: New advances and remaining questions. Science China Earth Sciences, 63, 1969–1991.

Yang, C.-H., Xu, W.-L., Yang, D.-B., Liu, C.-C., Liu, X.-M., and Hu, Z.-C. (2006) Petrogenesis of the Mesozoic high-Mg diorites in west Shandong: evidence from chronology and petro-geochemistry. Earth Science, 31, 81–92 (in Chinese with English abstract).

Yang, Y.-H., Wu, F.-Y., Wilde, S.A., Liu, X.-M., Zhang, Y.-B., Xie, L.-W., and Yang, J.-H. (2009) In situ perovskite Sr–Nd isotopic constraints on the petrogenesis of the Ordovician Mengyin kimberlites in the North China Craton. Chemical Geology, 264, 24–42.

Yang, D.-B., Xu, W.-L., Pei, F.-P., Yang, C.-H., and Wang, Q.-H. (2012a). Spatial extent of the influence of the deeply subducted South China Block on the southeastern North China Block: Constraints from Sr-Nd-Pb isotopes in Mesozoic mafic igneous rocks. Lithos, 136–139, 246–260.

Yang, Q.-L., Zhao, Z.-F., and Zheng, Y.-F. (2012b) Slab-mantle interaction in continental subduction channel: Geochemical evidence from Mesozoic gabbroic intrusives in southeastern North China. Lithos, 155, 442–460.

Yang, J.-H., Xu, L., Sun, J.-F., Zeng, Q.D., Zhao, Y.-N., Wang, H., and Zhu, Y.-S. (2021) Geodynamics of decratonization and related magmatism and mineralization in the North China Craton. Science China Earth Sciences, 64, 1409–1427.

Yogodzinski, G.M., Volynets, O.N., Koloskov, A.V., Seliverstov, N.I., and Matvenkov, V.V. (1994) Magnesian andesites and the subduction component in a strongly calc-alkaline series at Piip Volcano, Far Western Aleutians. Journal of Petrology, 35, 163–204.

Yogodzinski, G.M., Kay, R.W., Volynets, O.N., Koloskov, A.V., and Kay, S.M. (1995)

Magnesian andesite in the western Aleutian Komandorsky region: implications for slab melting and processes in the mantle wedge. Geological Society of America Bulletin, 107, 505–519.

Zhang, H.F., and Yang, Y.H. (2007) Emplacement age and Sr-Nd-Hf isotopic characteristics of the diamondiferous kimberlites from the eastern North China Craton. Acta Petrologica Sinica, 23(2), 285–294 (in Chinese with English abstract).

Zhang, J.-Q., Li, S.-R., Santosh, M., Wang, J.-Z., and Li, Q. (2015) Mineral chemistry of high-Mg diorites and skarn in the Han-Xing Iron deposits of South Taihang Mountains, China: Constraints on mineralization process. Ore Geology Reviews, 64, 200–214.

Zhang, C., Cui, F.H., Geng, R., Zhang, Z.L., Gao, M.B., and Gao, J.L. (2021) The Petrogenesis of Early Cretaceous Quartz Diorite in Skarn Iron Deposits, Jinling Area, Luxi : Evidence of Geochronology and Geochemistry. Mineralogy and Petrology, 41, 80–92 (in Chinese with English abstract).

Zhang, C., Ma, C., Holtz, F., 2010. Origin of high-Mg adakitic magmatic enclaves from the Meichuan pluton, southern Dabie orogen (central China): Implications for delamination of the lower continental crust and melt-mantle interaction. Lithos, 119, 467–484.

Zhao, G.C., Sun, M., Wilde, S.A., and Li, S.Z. (2005) Late Archean to Paleoproterozoic evolution of the North China Craton: key issues revisited. Precambrian Research, 136, 177–202.

Zheng, Y.-F., Xiao, W.-J., and Zhao, G.-C. (2013) Introduction to tectonics of China. Gondwana Research, 23, 1189–1206.

Zheng, Y.-F., Xu, Z., Chen, L., Dai, L.-Q., and Zhao, Z.-F. (2020) Chemical geodynamics of mafic magmatism above subduction zones. Journal of Asian Earth Sciences, 194, 104185.

Zhong, J.W., and Huang, X.L. (2012) Spatial variation of zircon Hf isotopes for the Early

Cretaceous mafic intrusions in western Shandong and its genesis. Geotectonica et Metallogenia, 36, 572–580 (in Chinese with English abstract).

Zhu, R.X., Chen, L., Wu, F.Y., and Liu, J.L. (2011) Timing, scale and mechanism of the destruction of the North China Craton. Science China Earth Sciences, 54, 789–797.

FIGURE CAPTIONS

Figure 1. (a) Geological sketch of the North China Craton (NCC) showing the distribution of major tectonic units and the location of Shandong Province (SDP). (b) Geological map of SDP and the location of the study area (modified from Huang et al. 2012). (c) Geological map of the Jinling high-Mg dioritic complex showing the distribution of the two groups of high-Mg dioritic rocks (modified from Zhong and Huang 2012). Abbreviations: DGTL, Daxinganling–Taihangshan Gravity Lineament; TLFZ, Tan–Lu fault zone; YTC, Yangtze Craton; CYB, Cathaysia Block; XMOB, Xing–Meng Orogenic Belt; SOB, Sulu Orogenic Belt; DOB, Dabie Orogenic Belt.

Figure 2. Petrographic characteristics of samples from the Jinling high-Mg dioritic complex. (a–c) Gabbroic diorites containing orthopyroxene and clinopyroxene phenocrysts rimmed by amphiboles. (d) Hornblende diorites containing core–rim-zoned amphibole phenocrysts with magnetite inclusions in the rim. Both amphiboles and plagioclases are common minerals in the matrix of gabbroic diorites and hornblende diorites. (e–f) Monzonites containing core–mantle–rim-zoned amphibole and plagioclase phenocrysts. Mineral abbreviations: Opx, orthopyroxene; Cpx, clinopyroxene; Amp, amphibole; Bi, biotite; Pl, plagioclase; Mt, magnetite.

Figure 3. Diagrams of (a) total alkalis versus SiO_2 and (b) K_2O versus SiO_2 for the Jinling high-Mg dioritic rocks from the Luxi area. Literature data are from Yang et al. (2006, 2012b), Jin et al. (2015), Lan et al. (2019), Gao et al. (2021), and Zhang et al. (2021). Abbreviations: PG, Peridotgabbro; FG, Foid gabbro; FMD, Foid monzodiorite; FMS, Foid monzosyenite; MG, Monzogabbro; MD, Monzodiorite; GD, Gabbroic diorite; QM, Quartz monzonite.

Figure 4. (a–i) Harker diagrams of major and trace elements for Jinling high-Mg dioritic rocks from the Luxi area. Literature data sources are the same as for Fig. 3. The

fields of > 3.5 Ga TTG and < 3.0 Ga TTG are after Martin et al. (2005).

Figure 5. (a) Chondrite-normalized REE diagram and (b) primitive-mantle-normalized multi-element variation diagram for the Jinling high-Mg dioritic rocks from the Luxi area. Normalization values are from McDonough and Sun (1995). Literature data sources are the same as for Fig. 3.

Figure 6. Histograms of (a) zircon U–Pb ages and (b) zircon $\varepsilon_{Hf}(t)$ values and (c) diagram of whole-rock $\varepsilon_{Nd}(t)$ versus $(^{87}Sr/^{86}Sr)_i$ for the Jinling high-Mg dioritic rocks from the Luxi area. The field for sub-continental lithospheric mantle (SCLM) of the North China Craton is after Zhang and Yang (2007) and Yang et al. (2009); data for the Taishan Group TTG gneisses are from Jahn et al. (1988), Peng et al. (2013), and Chen et al. (2020). Literature data for the Jinling high-Mg dioritic rocks are from Yang et al. (2006, 2012b), Zhong and Huang (2012), Jin et al. (2015), Lan et al. (2019), Gao et al. (2021), and Zhang et al. (2021).

Figure 7. (a–b) Back-scattered electron images of plagioclase in (a) Group-I and (b) Group-II high-Mg dioritic rocks. (c) An–Ab–Or ternary diagram for plagioclase from the Jinling high-Mg dioritic rocks of the Luxi area. Red circles indicate EPMA analytical spots, and numbers adjacent to circles are An contents. Mineral abbreviations are the same as for Fig. 2.

Figure 8. (a–b) Back-scattered electron images of amphibole phenocrysts in (a) Group-I (adapted from Guo et al. 2022) and (b) Group-II high-Mg dioritic rocks. (c–d) Classification of amphiboles from the Jinling high-Mg dioritic rocks of the Luxi area. Red circles indicate EPMA analytical spots, and numbers adjacent to circles are Al_2O_3 contents. Major-element data for amphiboles from Group-I high-Mg dioritic rocks are from Guo et al. (2022). Mineral abbreviations are the same as for Fig. 2.

Figure 9. Diagrams of (a) Mg# versus SiO_2 (modified after Rapp et al. 1999), (b) TiO_2 versus $MgO/(MgO + FeO^T)$ (modified after Kemei et al. 2004), (c) Sr/Y versus Y (modified after Defant and Drummond 1990), and (d) Sr/Y versus Y (modified after Kemei et al. 2004) for the Jinling high-Mg dioritic rocks from the Luxi area. The experimental melt compositions are from Hirose (1997). The plot regions of Sanukitic, Adakitic, Bajaitic and Boninitic HMAs are from Kemei et al. (2004), and other literature data sources are the same as for Fig. 3.

Figure 10. Diagrams of (a) La/Sm versus La, (b) $(Hf/Sm)_N$ versus $(Ta/La)_N$ (modified after LaFlèche et al. 1998), (c) whole-rock $(^{87}Sr/^{86}Sr)_i$ versus $(La/Yb)_N$, and (d) whole-rock $\varepsilon_{Nd}(t)$ versus Sr/Y for the Jinling high-Mg dioritic rocks from the Luxi area. Data for the Taishan Group TTG gneisses are from Jahn et al. (1988), Peng et al. (2013), and Chen et al. (2020). Other literature data sources are the same as for Fig. 3. Abbreviations: DM, depleted mantle; N-MORB, normal mid-oceanic ridge basalt; OIB, oceanic island basalt.

Figure 11. Diagrams of (a) Si–Ti–Al ternary (modified after Jiang and An 1984), (b) TiO_2 versus Al_2O_3 (modified after Sun et al. 2019), and (c) (Na + K) versus Al^{IV} (modified after Jiang and An 1984) for amphiboles from the Jinling high-Mg dioritic rocks of the Luxi area. Major-element data for amphiboles from the Group-I high-Mg dioritic rocks are from Guo et al. (2022).

Figure 12. Diagrams of (a) P versus T, (b) $\log(fO_2)$ versus T, (c) T versus H_2O_{melt}, and (d) $Fe^{3+}/(Fe^{3+} + Fe^{2+})$ versus ΔNNO for amphiboles from the Jinling high-Mg dioritic rocks of the Luxi area (modified after Ridolfi et al. 2010). Fields for the cores of amphibole phenocrysts (I) and rims of amphibole phenocrysts and matrix amphiboles (II) of high-Mg dioritic rocks from the Han–Xing district are from Zhang et al. (2015).

DOI: https://doi.org/10.2138/am-2022-8755. http://www.minsocam.org/

Figure 13. Schematic model for the petrogenetic relationship between the Group-I and Group-II high-Mg dioritic rocks of the Jinling complex in the Luxi area (modified after Guo et al. 2022). Abbreviations: SCLM, sub-continental lithospheric mantle of the North China Craton; Amp, amphibole; Pl, plagioclase.

Figure 1

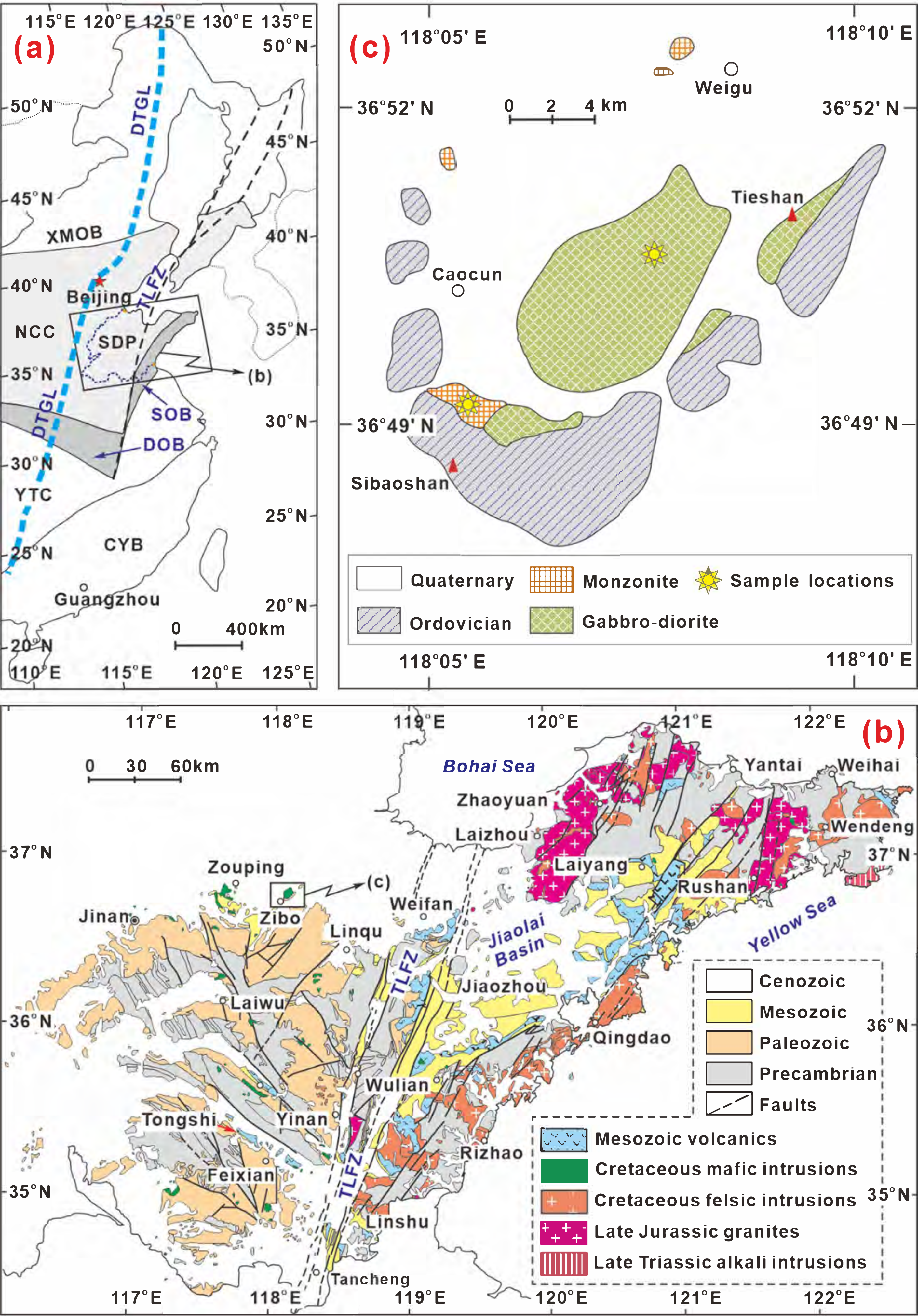
(a)
115°E 120°E 125°E 130°E 135°E
50°N
45°N
40°N
35°N
30°N
25°N
20°N
DTGL
XMOB
TLFZ
Beijing
NCC
SDP
SOB
DOB
YTC
CYB
Guangzhou
0 400km
110°E 115°E 120°E 125°E
(b)
(c)
118°05' E
118°10' E
36°52' N
36°49' N
0 2 4 km
Weigu
Tieshan
Caocun
Sibaoshan
Quaternary
Monzonite
Sample locations
Ordovician
Gabbro-diorite
117°E 118°E 119°E 120°E 121°E 122°E
37°N
36°N
35°N
0 30 60km
Bohai Sea
Yantai
Weihai
Zhaoyuan
Laizhou
Wendeng
Laiyang
Rushan
Zouping
Zibo
Jinan
Weifan
Linqu
Jiaolai Basin
Yellow Sea
Jiaozhou
Laiwu
Qingdao
Wulian
Tongshi
Yinan
Rizhao
Feixian
Linshu
Tancheng
Cenozoic
Mesozoic
Paleozoic
Precambrian
Faults
Mesozoic volcanics
Cretaceous mafic intrusions
Cretaceous felsic intrusions
Late Jurassic granites
Late Triassic alkali intrusions

Figure 2

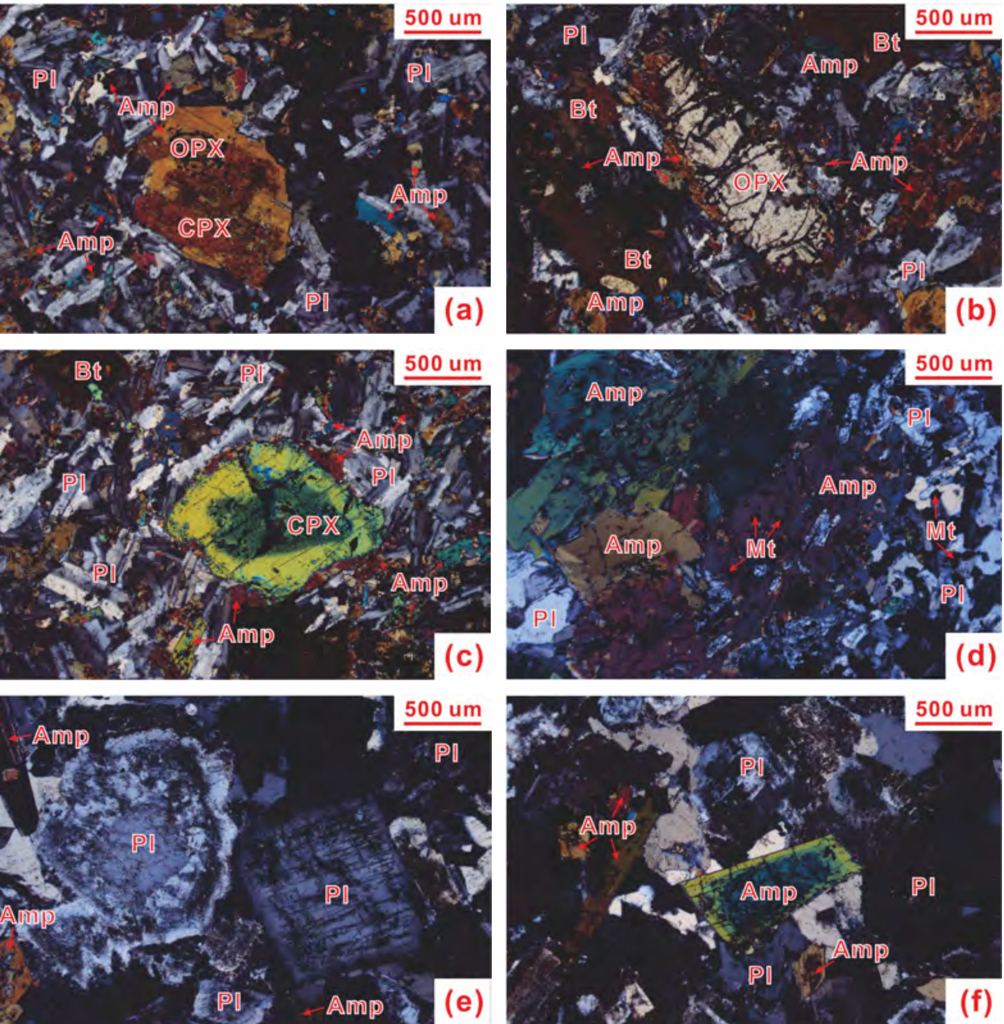

Figure 3

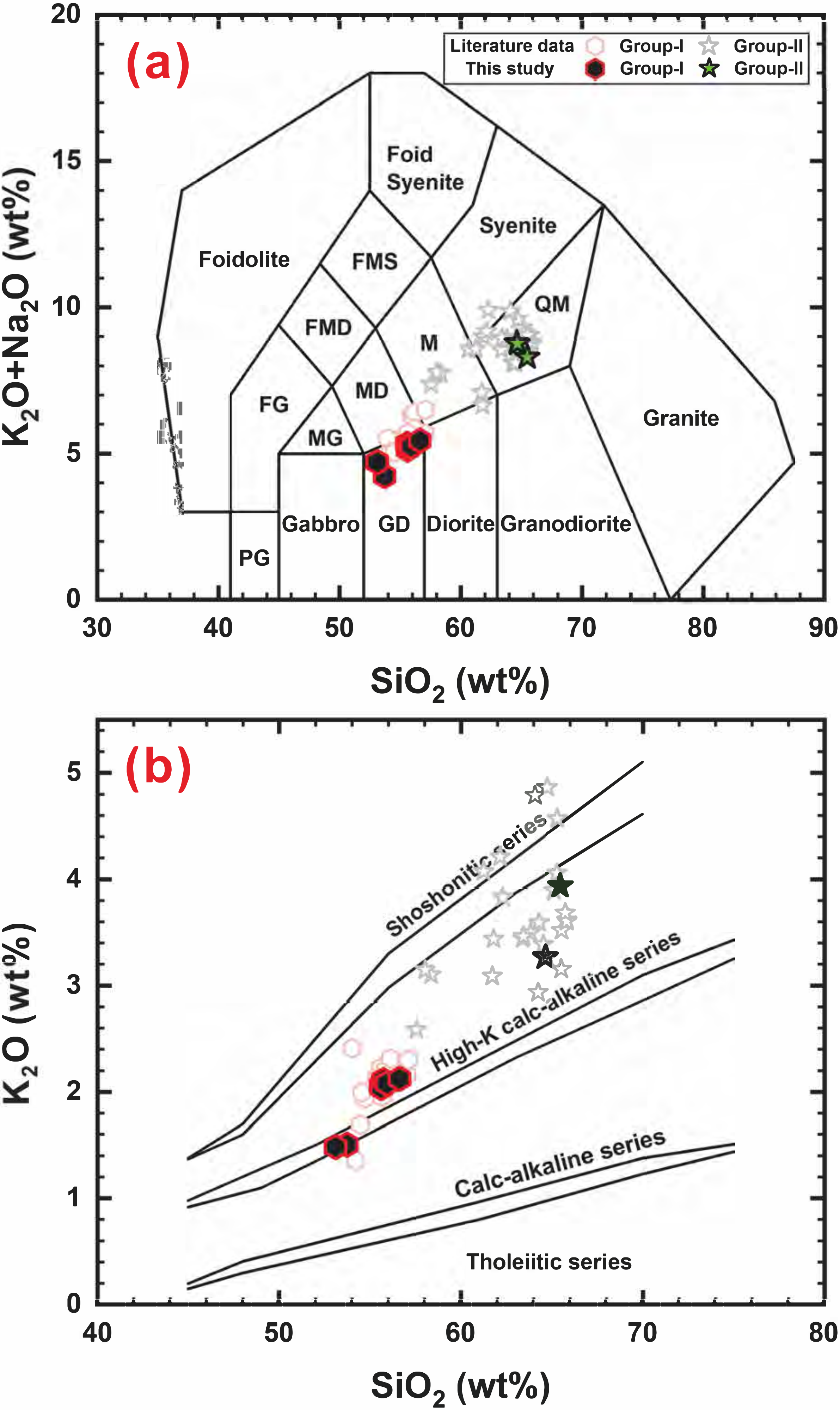
(a)
Literature data
This study
Group-I
Group-II
Group-I
Group-II
Foid Syenite
Syenite
Foidolite
FMS
FMD
QM
M
MD
FG
MG
Granite
Gabbro
GD
Diorite
Granodiorite
PG
K_2O+Na_2O (wt%)
SiO_2 (wt%)
(b)
Shoshonitic series
High-K calc-alkaline series
Calc-alkaline series
Tholeiitic series
K_2O (wt%)
SiO_2 (wt%)

Figure 4

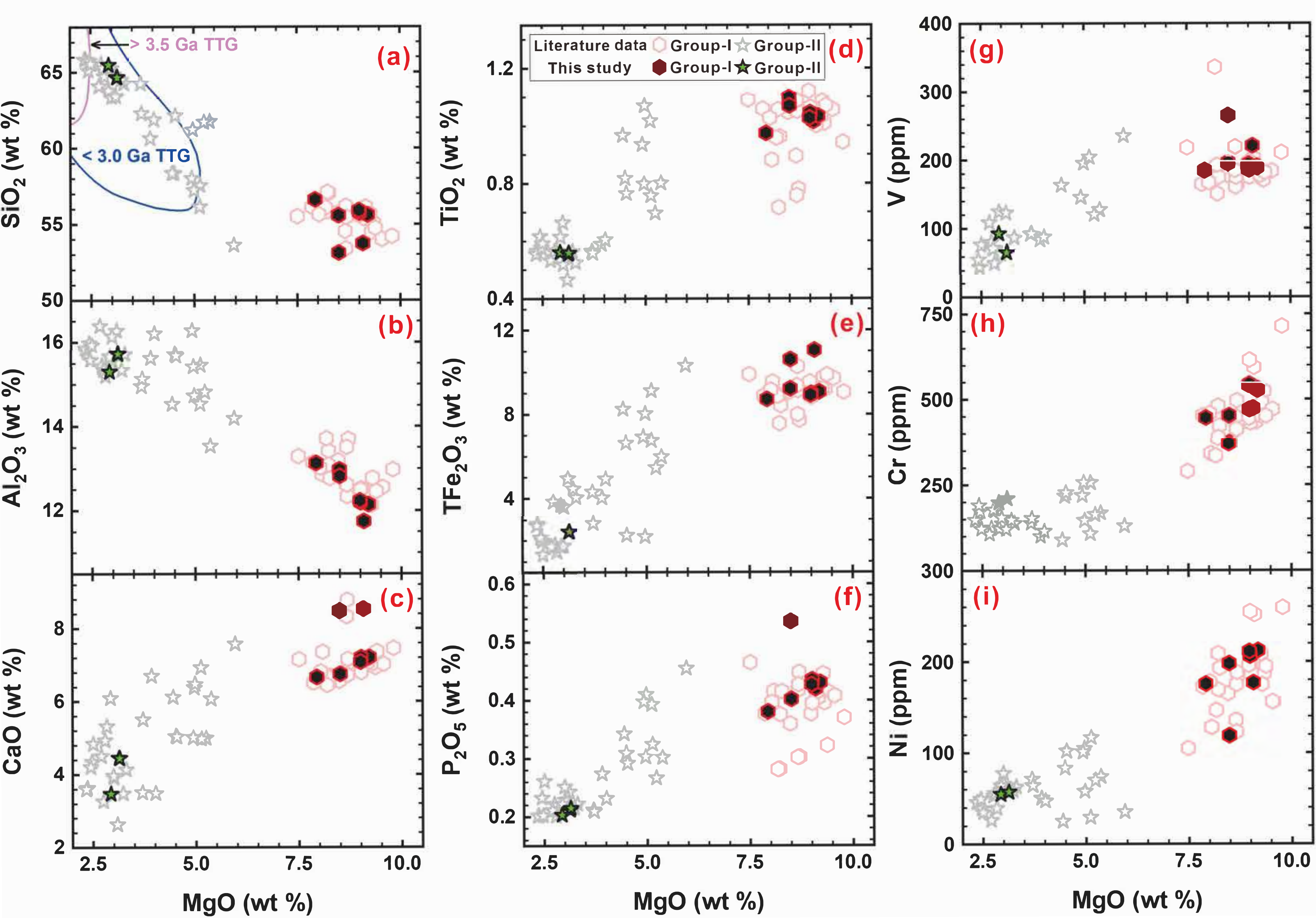

> 3.5 Ga TTG
< 3.0 Ga TTG
(a)
SiO2 (wt %)
(b)
Al2O3 (wt %)
(c)
CaO (wt %)
MgO (wt %)
Literature data
Group-I
Group-II
This study
Group-I
Group-II
(d)
TiO2 (wt %)
(e)
TFe2O3 (wt %)
(f)
P2O5 (wt %)
MgO (wt %)
(g)
V (ppm)
(h)
Cr (ppm)
(i)
Ni (ppm)
MgO (wt %)

Figure 5

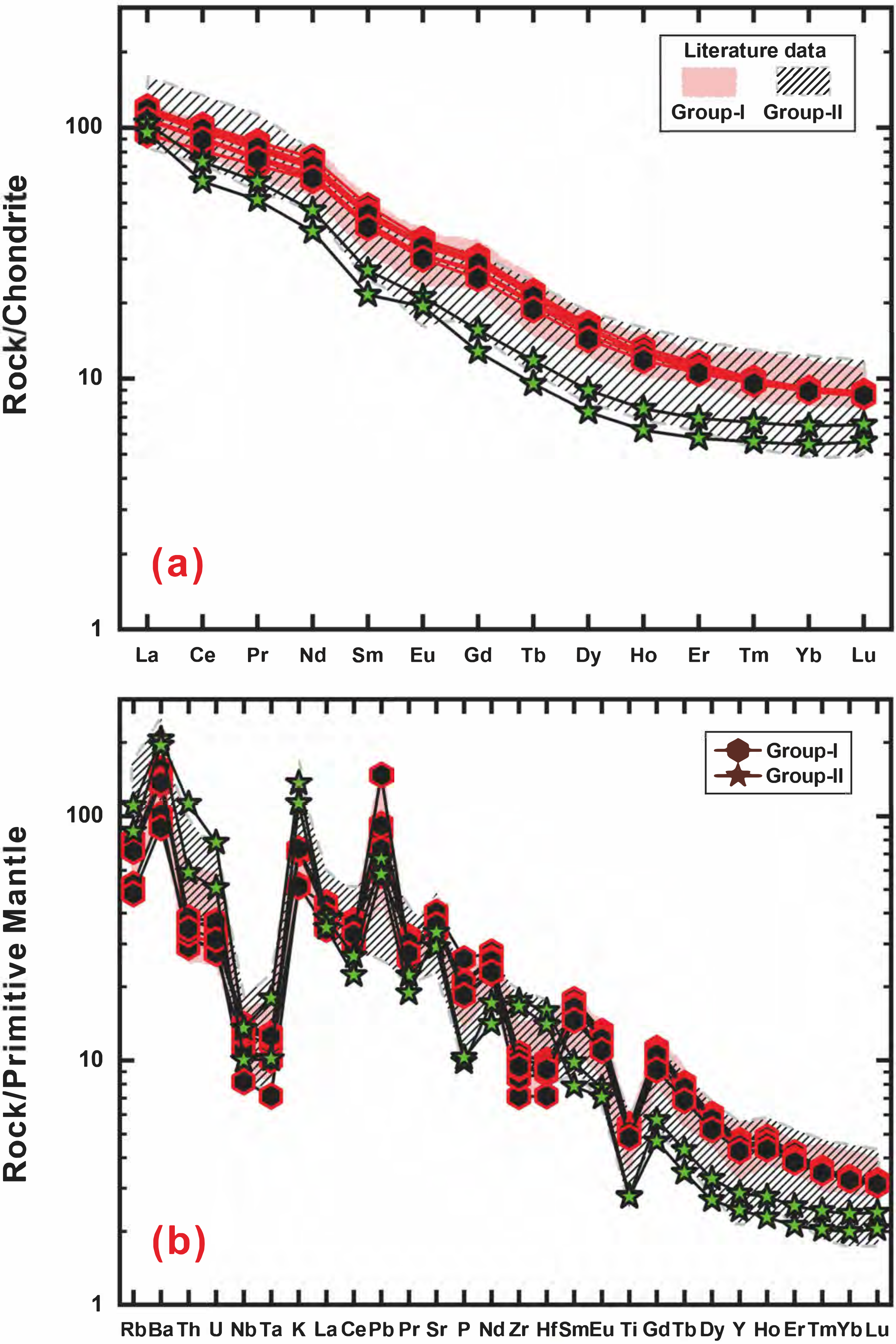

Literature data
Group-I
Group-II
100
10
1
Rock/Chondrite
(a)
La
Ce
Pr
Nd
Sm
Eu
Gd
Tb
Dy
Ho
Er
Tm
Yb
Lu
Group-I
Group-II
100
10
1
Rock/Primitive Mantle
(b)
Rb Ba Th U Nb Ta K La Ce Pb Pr Sr P Nd Zr Hf Sm Eu Ti Gd Tb Dy Y Ho Er Tm Yb Lu

Figure 6

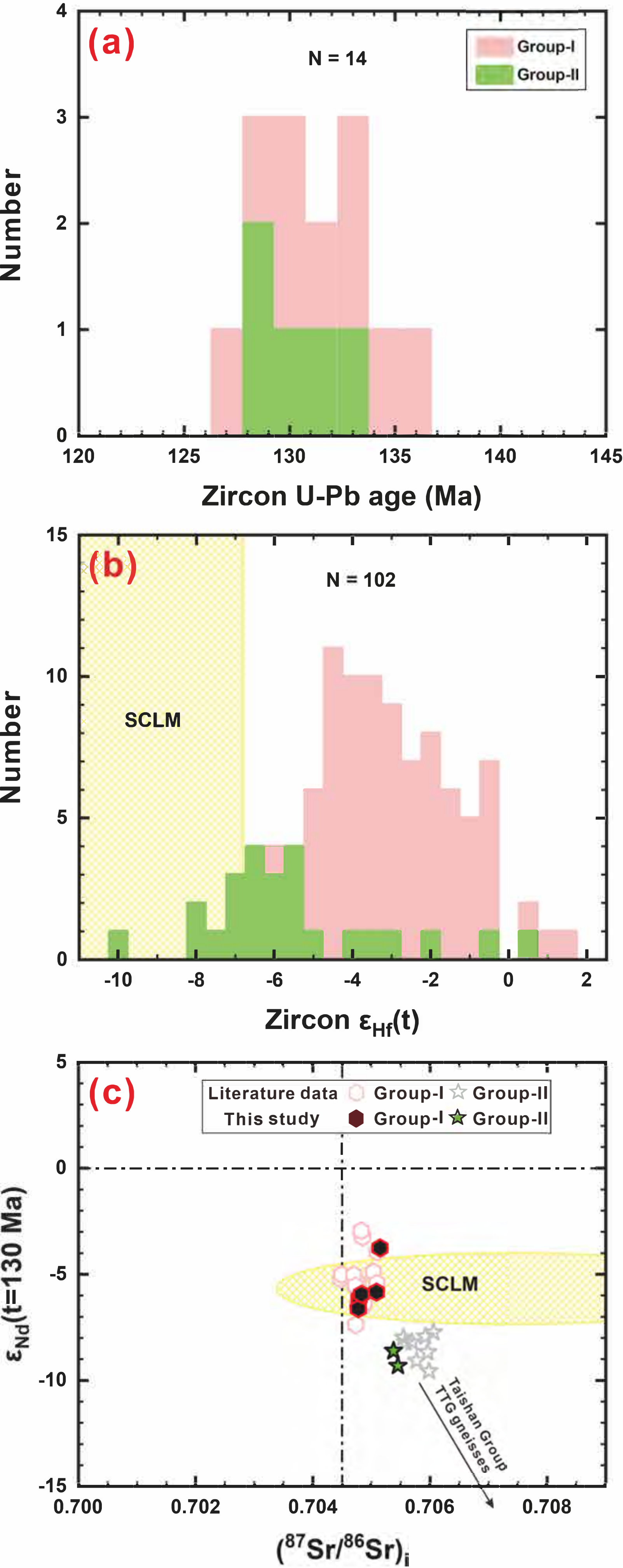

(a)
N = 14
Group-I
Group-II
Number
4
3
2
1
0
120
125
130
135
140
145
Zircon U-Pb age (Ma)
(b)
N = 102
SCLM
Number
15
10
5
0
-10
-8
-6
-4
-2
0
2
Zircon $\varepsilon_{Hf}(t)$
(c)
Literature data
Group-I
Group-II
This study
Group-I
Group-II
SCLM
Taishan Group
TTG gneisses
$\varepsilon_{Nd}(t=130\ Ma)$
5
0
-5
-10
-15
0.700
0.702
0.704
0.706
0.708
$(^{87}Sr/^{86}Sr)_i$

Figure 7

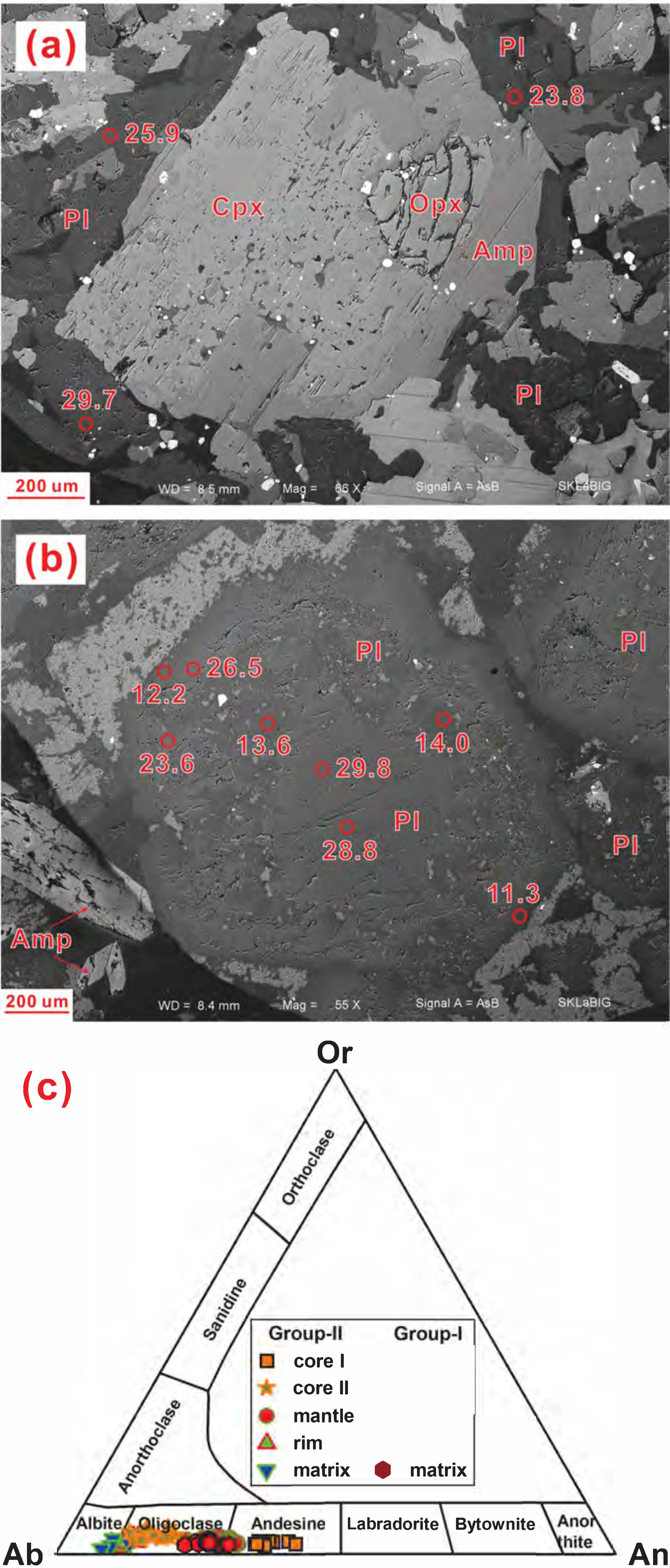
(a)
Pl
23.8
25.9
Pl
Cpx
Opx
Amp
Pl
29.7
200 um
WD = 8.5 mm
Mag = 66 X
Signal A = AsB
SKLaBIG
(b)
Pl
26.5
12.2
13.6
14.0
23.6
29.8
Pl
28.8
Pl
Pl
11.3
Amp
200 um
WD = 8.4 mm
Mag = 55 X
Signal A = AsB
SKLaBIG
(c)
Or
Orthoclase
Sanidine
Anorthoclase
Group-II
Group-I
core I
core II
mantle
rim
matrix
matrix
Albite
Oligoclase
Andesine
Labradorite
Bytownite
Anorthite
Ab
An

Figure 8

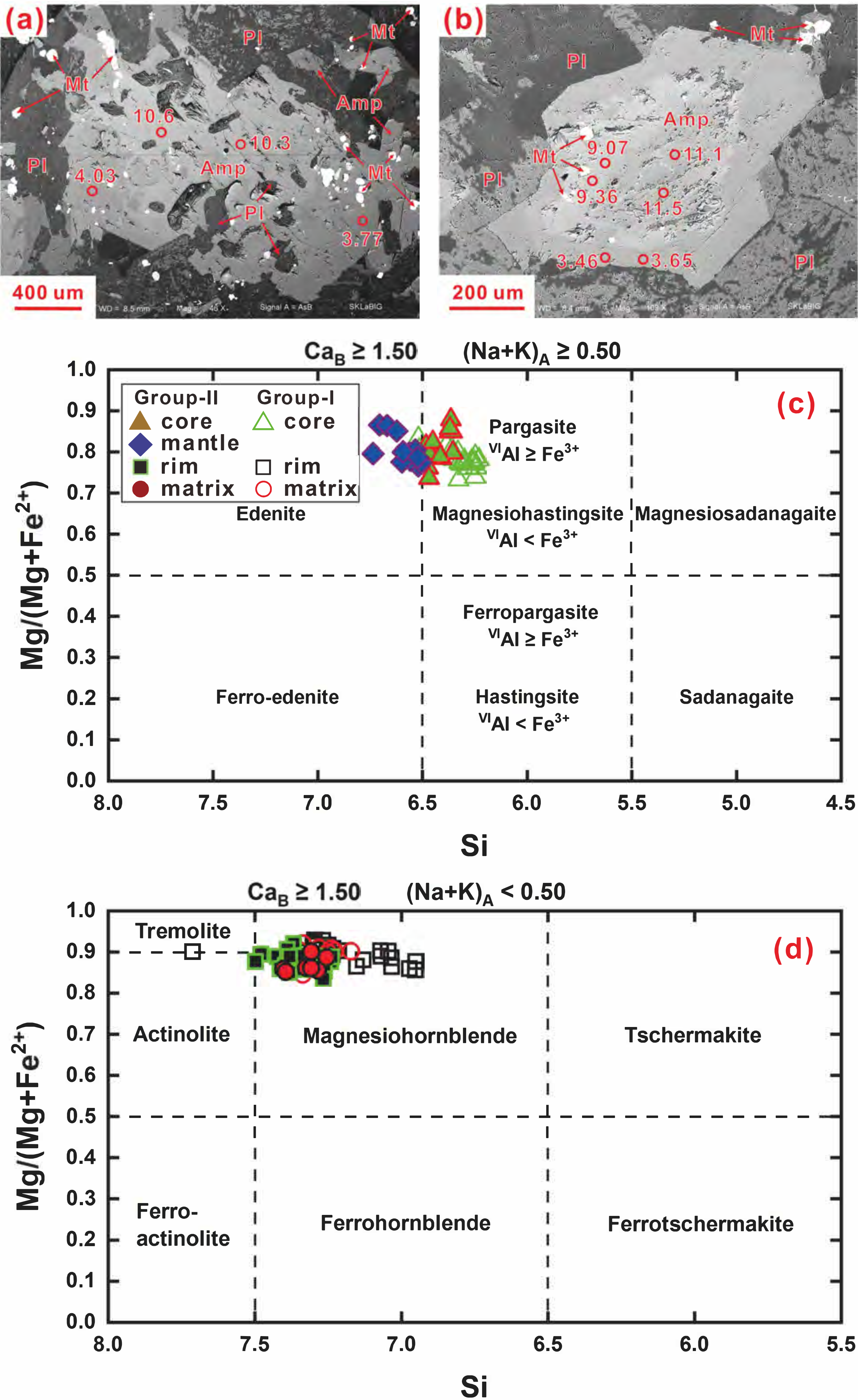

(a)
Pl
Mt
Amp
10.6
10.3
4.03
3.77
400 um
(b)
Pl
Mt
Amp
9.07
9.36
11.1
11.5
3.46
3.65
200 um
$Ca_B \geq 1.50$ $(Na+K)_A \geq 0.50$
(c)
Group-II
Group-I
core
mantle
rim
matrix
Pargasite
$^{VI}Al \geq Fe^{3+}$
Edenite
Magnesiohastingsite
$^{VI}Al < Fe^{3+}$
Magnesiosadanagaite
Ferropargasite
$^{VI}Al \geq Fe^{3+}$
Ferro-edenite
Hastingsite
$^{VI}Al < Fe^{3+}$
Sadanagaite
$Mg/(Mg+Fe^{2+})$
Si
$Ca_B \geq 1.50$ $(Na+K)_A < 0.50$
(d)
Tremolite
Actinolite
Magnesiohornblende
Tschermakite
Ferro-actinolite
Ferrohornblende
Ferrotschermakite
$Mg/(Mg+Fe^{2+})$
Si

Figure 9

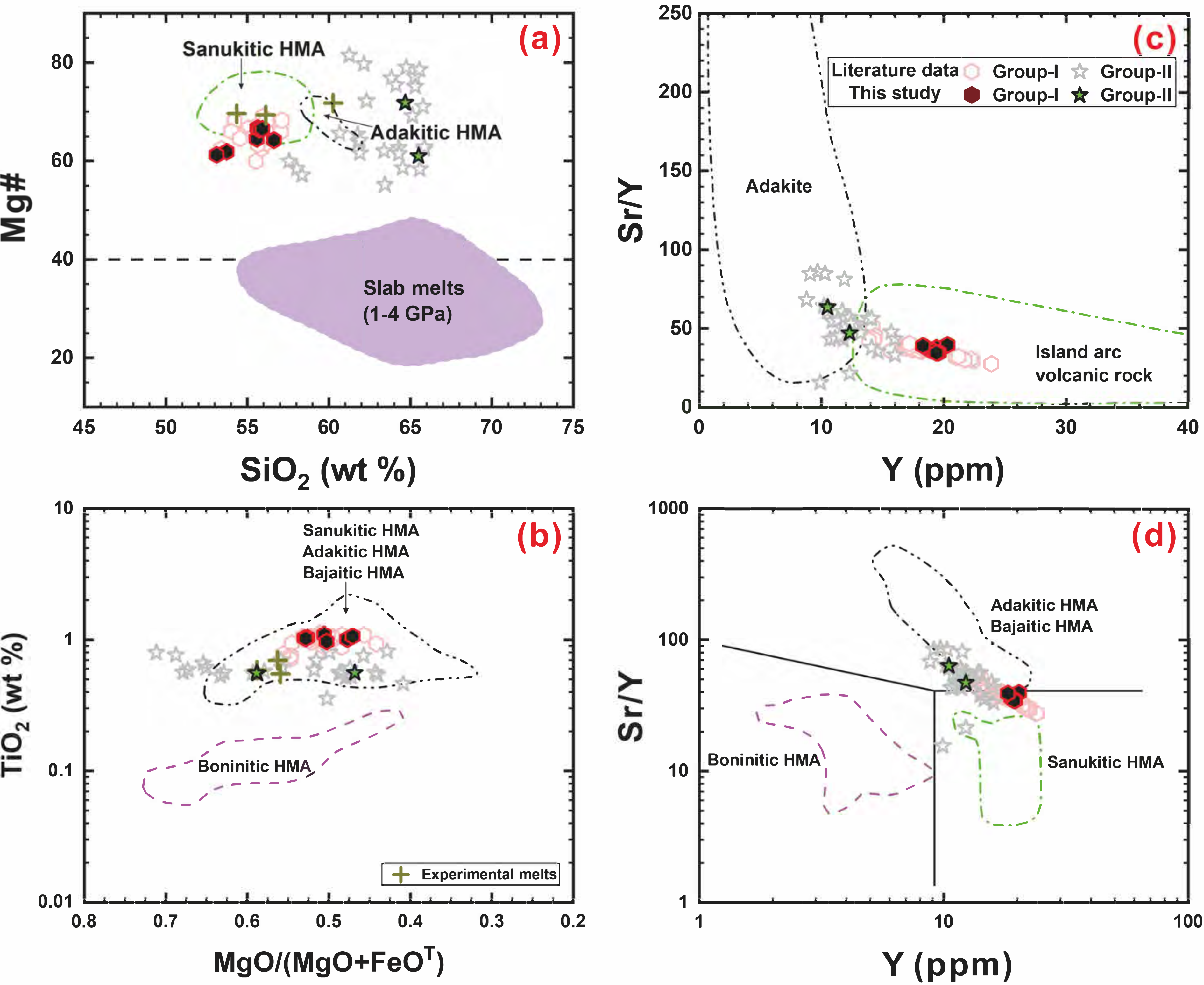

(a)
Sanukitic HMA
Adakitic HMA
Slab melts
(1-4 GPa)
Mg#
SiO2 (wt %)
(c)
Literature data
This study
Group-I
Group-II
Group-I
Group-II
Adakite
Island arc
volcanic rock
Sr/Y
Y (ppm)
(b)
Sanukitic HMA
Adakitic HMA
Bajaitic HMA
Boninitic HMA
Experimental melts
TiO2 (wt %)
MgO/(MgO+FeOT)
(d)
Adakitic HMA
Bajaitic HMA
Boninitic HMA
Sanukitic HMA
Sr/Y
Y (ppm)

Figure 10

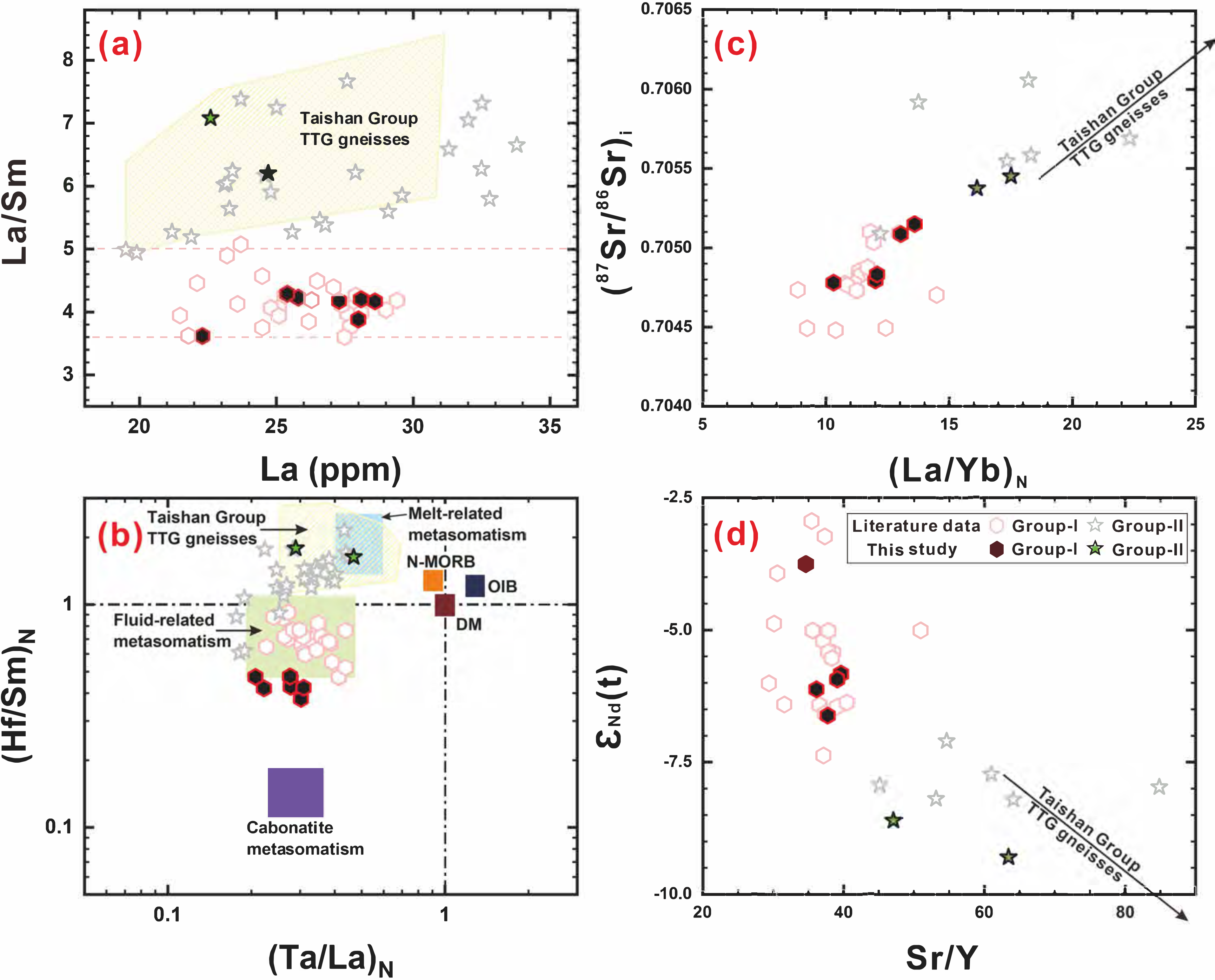

(a)
Taishan Group
TTG gneisses
La/Sm
La (ppm)
(b)
Taishan Group
TTG gneisses
Melt-related
metasomatism
N-MORB
OIB
DM
Fluid-related
metasomatism
Cabonatite
metasomatism
$(Hf/Sm)_N$
$(Ta/La)_N$
(c)
Taishan Group
TTG gneisses
$(^{87}Sr/^{86}Sr)_i$
$(La/Yb)_N$
(d)
Literature data
Group-I
Group-II
This study
Group-I
Group-II
Taishan Group
TTG gneisses
$\varepsilon_{Nd}(t)$
Sr/Y

Figure 11

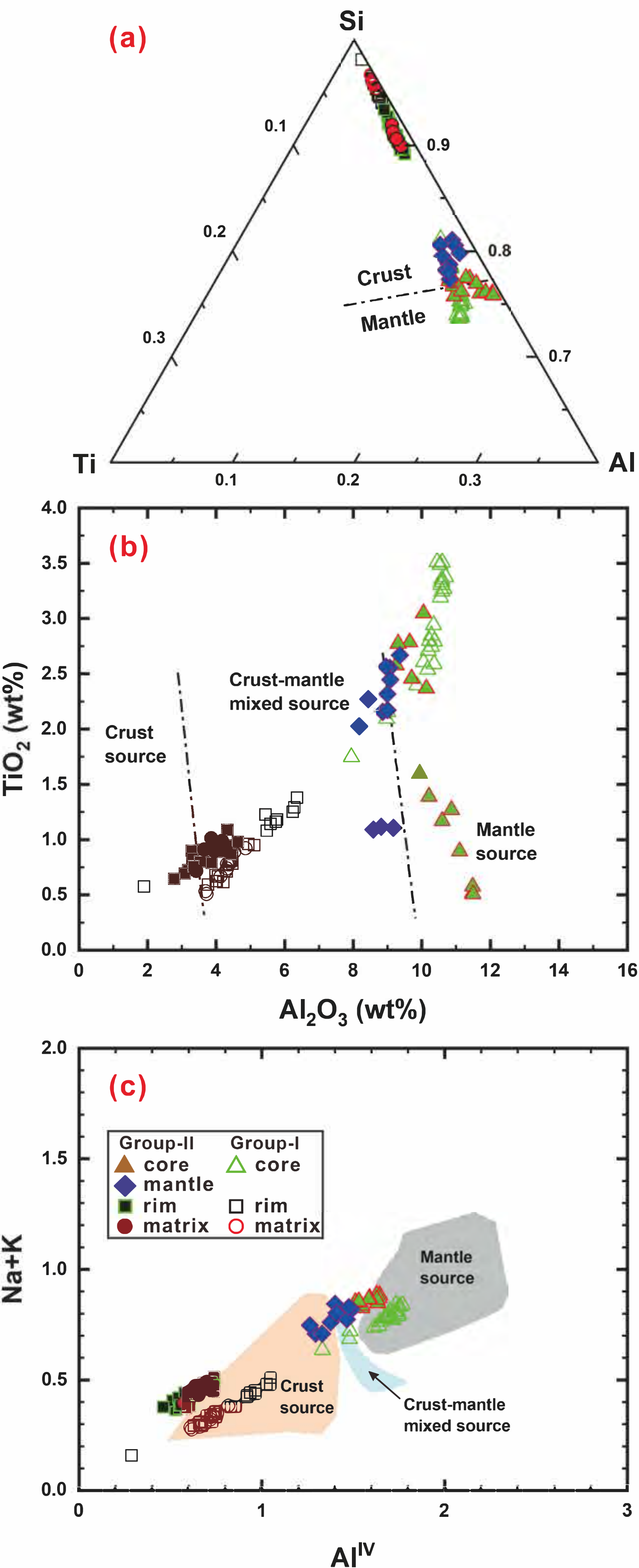

(a)
Si
Ti
Al
0.1
0.2
0.3
0.9
0.8
0.7
Crust
Mantle
(b)
Crust source
Crust-mantle mixed source
Mantle source
TiO2 (wt%)
Al2O3 (wt%)
(c)
Group-II
Group-I
core
mantle
rim
matrix
Mantle source
Crust source
Crust-mantle mixed source
Na+K
AlIV

Figure 12

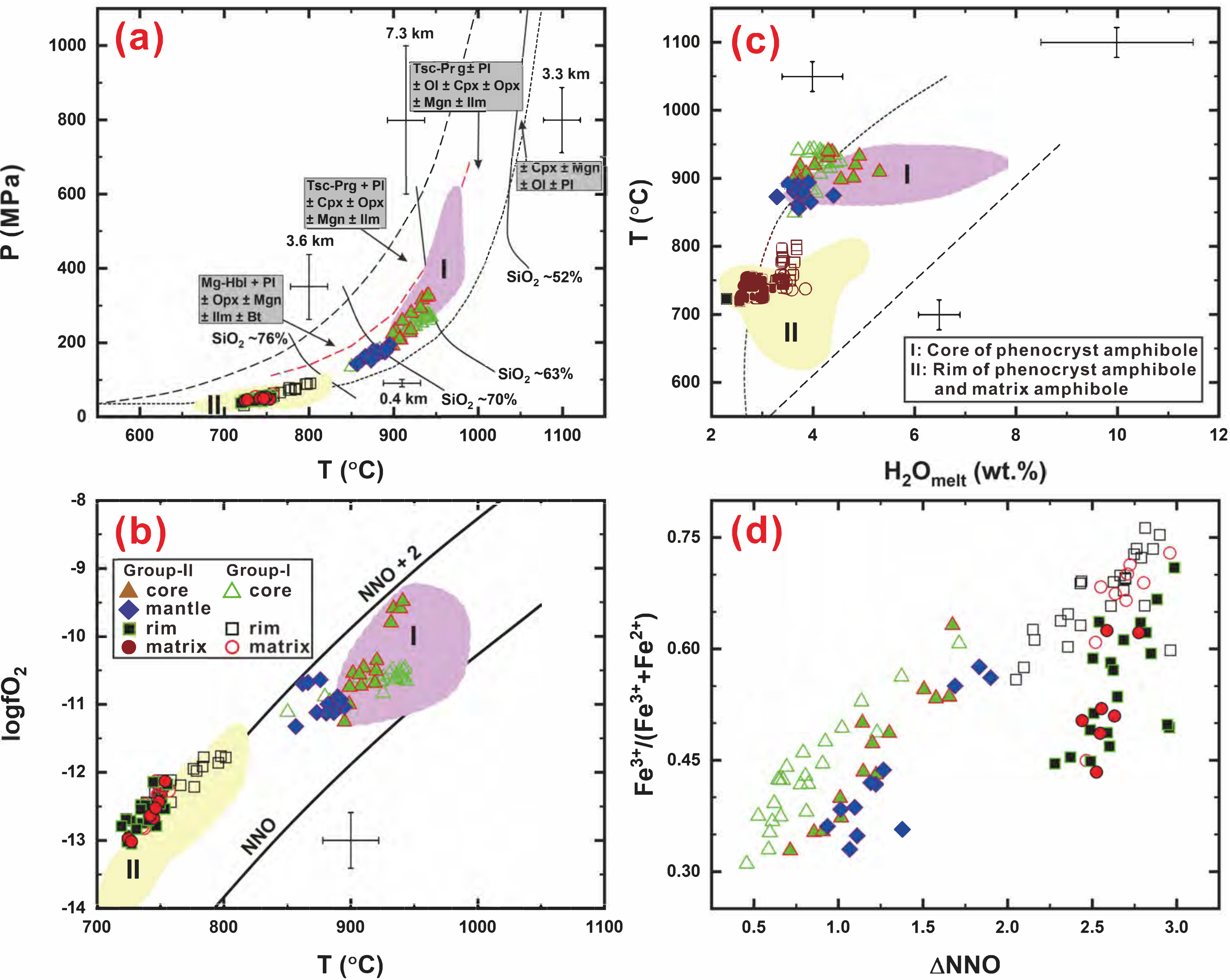

(a)
7.3 km
3.3 km
3.6 km
0.4 km
Tsc-Prg ± Pl
± Ol ± Cpx ± Opx
± Mgn ± Ilm
Tsc-Prg + Pl
± Cpx ± Opx
± Mgn ± Ilm
Mg-Hbl + Pl
± Opx ± Mgn
± Ilm ± Bt
± Cpx ± Mgn
± Ol ± Pl
SiO_2 ~52%
SiO_2 ~63%
SiO_2 ~70%
SiO_2 ~76%
I
II
P (MPa)
T (°C)
(c)
I
II
I: Core of phenocryst amphibole
II: Rim of phenocryst amphibole
and matrix amphibole
T (°C)
H_2O_{melt} (wt.%)
(b)
Group-II
core
mantle
rim
matrix
Group-I
core
rim
matrix
NNO + 2
NNO
I
II
$\log fO_2$
T (°C)
(d)
$Fe^{3+}/(Fe^{3+}+Fe^{2+})$
ΔNNO

Figure 13

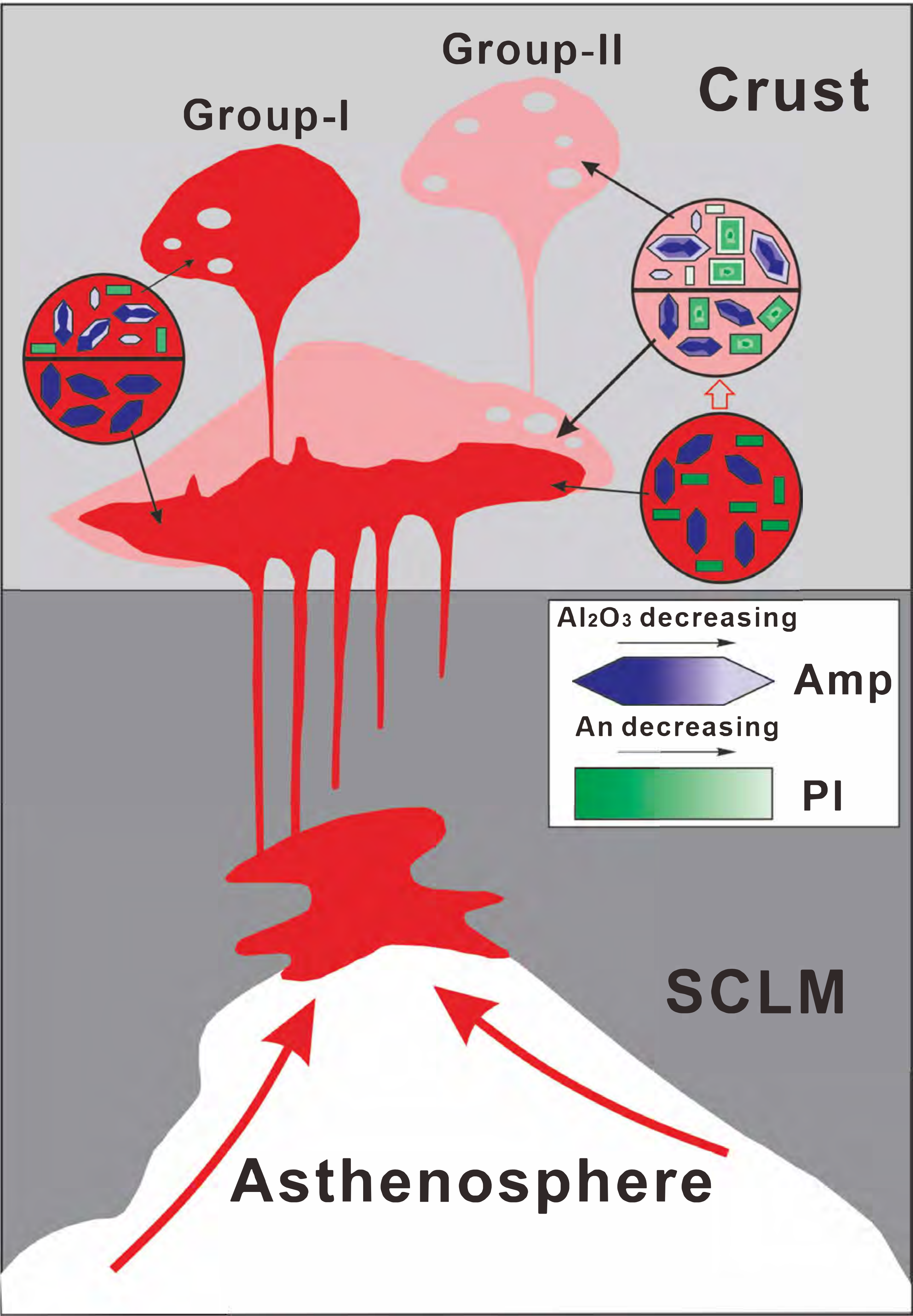
Group-II
Crust
Group-I
Al2O3 decreasing
Amp
An decreasing
Pl
SCLM
Asthenosphere